Atmos. Chem. Phys. Discuss., 14, 3815–3874, 2014
www.atmos-chem-phys-discuss.net/14/3815/2014/
doi:10.5194/acpd-14-3815-2014

Atmospheric Chemistry and Physics Discussions

The thermodynamic structure of summer Arctic stratocumulus and the dynamic coupling to the surface

G. Sotiropoulou[1,2], J. Sedlar[1,2], M. Tjernström[1,2], M. D. Shupe[3,4], I. M. Brooks[5], and P. O. G. Persson[3,4]

[1]Department of Meteorology, Stockholm University, Stockholm, Sweden
[2]Bert Bolin Center for Climate Research, Stockholm University, Stockholm, Sweden
[3]Cooperative Institute for Research in the Environmental Sciences, University of Colorado, Boulder, Colorado, USA
[4]NOAA Earth System Research Laboratory, Boulder, Colorado, USA
[5]Institute for Climate and Atmospheric Science, School of Earth and Environment, University of Leeds, Leeds, UK

Received: 16 December 2013 – Accepted: 28 January 2014 – Published: 11 February 2014

Correspondence to: G. Sotiropoulou (georgia@misu.su.se)

Published by Copernicus Publications on behalf of the European Geosciences Union.

Abstract

The vertical structure of Arctic low-level clouds and Arctic boundary layer is studied, using observations from ASCOS (Arctic Summer Cloud Ocean Study), in the central Arctic, in late summer 2008. Two general types of cloud structures are examined: the "neutrally-stratified" and "stably-stratified" clouds. Neutrally-stratified are mixed-phase clouds where radiative-cooling near cloud top produces turbulence that creates a cloud-driven mixed layer. When this layer mixes with the surface-generated turbulence, the cloud layer is coupled to the surface, whereas when such an interaction does not occur, it remains decoupled; the latter state is most frequently observed. The decoupled clouds are usually higher compared to the coupled; differences in thickness or cloud water properties between the two cases are however not found. The surface fluxes are also very similar for both states. The decoupled clouds exhibit a bimodal thermodynamic structure, depending on the depth of the sub-cloud mixed layer (SML): clouds with shallower SMLs are disconnected from the surface by weak inversions, whereas those that lay over a deeper SML are associated with stronger inversions at the decoupling height. Neutrally-stratified clouds generally precipitate; the evaporation/sublimation of precipitation often enhances the decoupling state. Finally, stably-stratified clouds are usually lower, geometrically and optically thinner, non-precipitating liquid-water clouds, not containing enough liquid to drive efficient mixing through cloud-top cooling.

1 Introduction

Rapid changes in the Arctic climate during the past decades (Serreze et al., 2000; Overland et al., 2004; ACIA, 2005) have led to widespread attention in the global climate research community. Annual average near-surface temperatures in the Arctic have increased by over a factor of two compared to the rest of the world (ACIA 2005; Richter-Menge, 2010) and the sea-ice extent has been declining at an acceler-

ACPD
14, 3815–3874, 2014

ating rate, especially during summer and early fall (Comiso, 2002; Nghiem et al., 2007; Stroeve et al., 2012). Extreme anomalies in the mid-September ice extent minima over the last decade (Serreze et al., 2007; Stroeve et al., 2012), including record minima in 2007 (Maslanik et al., 2007; Lindsay et al., 2009) and 2012 (Simmonds and Rudeva, 2012; Devasthale et al., 2013; Zhang et al., 2013) are indicative of an increasing "Arctic amplification" (Serreze and Francis, 2006; Serreze and Berry, 2011) signaling rapid climate change. This amplification has been attributed to several factors that affect the surface energy budget; one of the most important of them is the surface-albedo feedback (Perovich et al., 2008; Stroeve et al., 2012) and how changes at the surface impact the cloud response (Kay and Gettelman, 2009). Other hypotheses also exist, for example that changes in the large-scale Northern Hemisphere atmospheric circulation (Graversen et al., 2008; Kapsch et al., 2013) and convergent meridional heat transport may explain changes in the clouds and hence the surface energy balance.

To understand the Arctic climate system, a detailed understanding of cloud processes and their impact on both the surface and atmospheric thermodynamic structure are required (Curry et al., 1996). In general, solar radiation is reflected by clouds, leading to a radiative cooling at the surface, whereas longwave radiation is both absorbed and emitted by clouds. Over the Arctic, where surface albedo and solar zenith angles are relatively large and clouds are predominantly low, the net effect on the sea ice surface is a warming (Shupe and Intrieri, 2004; Sedlar et al., 2011), except possibly for a short period in summer, when the surface albedo is reduced by melting (Intrieri et al., 2002). The influence of the clouds on the surface energy budget depends on several parameters, such as the cover, phase, and vertical and horizontal cloud distribution, etc. (Randall et al., 1998); combining all the factors is complex and it is no surprise that clouds are very difficult to model. In particular, global climate models exhibit a large variation in global and regional sensitivity to imposed large-scale forcing, which has been largely attributed to differences in cloud feedbacks and especially those of low-level clouds (Bony and Dufresne, 2005; Webb et al., 2006; Lauer et al., 2010).

ACPD
14, 3815–3874, 2014

Low-level clouds occur very frequently in the Arctic, especially during the summer half of the year when they occur for 80–90 % of the time (Curry and Ebert, 1992; Wang and Key, 2005; Tjernström, 2005; Shupe et al., 2011; Liu et al., 2012). Clouds below 3 km a.s.l. (above surface level; unless otherwise stated all heights will be given above the surface) over the Arctic are most frequently mixed phase, consisting of both droplets and ice crystals together in the same volume (Shupe, 2011); the liquid is often concentrated in a thin layer near the top of the cloud, continuously precipitating frozen drizzle or ice crystals formed within the liquid layer (Shupe et al., 2008). These clouds have been observed to persist for long durations – hours to days (Shupe et al., 2011) – and are believed to have a critical impact on the surface energy balance (Intrieri et al., 2002; Persson et al., 2002; Shupe and Intrieri, 2004; Sedlar et al., 2011). Both short- and longwave radiation are very sensitive to cloud phase; longwave opacity increases asymptotically to unity with cloud liquid water path, while shortwave reflection to space increases with increasing numbers of smaller, spherical cloud droplets (e.g., Twomey, 1977; Stephens, 1978). The end result is significantly more longwave radiation emitted to the surface and less shortwave radiation transmitted to the surface when liquid droplets are present than for ice only clouds (Prenni et al., 2007).

Mixed-phase clouds particularly are poorly handled by current climate models (Tjernström et al., 2005, 2008; Karlsson and Svensson, 2010), suggesting the processes that support the maintenance of these clouds in the Arctic are not fully understood. These processes are discussed in Morrison et al. (2012). For example, turbulence generated by cloud-top cooling and in-cloud upward air motion are considered to play a critical role; the layer with largest liquid concentrations near cloud top emits longwave radiation to space (Pinto, 1998), which decreases static stability in the clouds and leads to buoyant overturning circulation (e.g., Nicholls, 1984). These cloud-driven turbulent motions promote the growth of both liquid and ice, rather than just ice growing at the expense of the liquid (Korolev, 2007) as would intuitively be expected in an ice/liquid mixture. Moreover, mixing from below cloud base may also be ongoing, driven by surface forcing and/or advection in the lower troposphere, leading to an upward transfer

ACPD
14, 3815–3874, 2014

of heat and moisture. The coupling, or lack thereof (hence referred to as decoupling), between cloud- and surface-generated turbulence may be critically important for the sustenance of mixed-phase clouds.

Because of the strongly stable near-surface conditions that often occur during winter to early spring (Kahl, 1992; Curry, 1986), surface fluxes are often considered to have no significant contribution to the cloud's moisture during these seasons; this changes from late spring until October when the open ice-free ocean and melting sea ice exposes a large source of heat and moisture to the relatively cool and dry lower atmosphere (Pinto and Curry, 1995). Analysis of the vertical atmospheric structure in late summer from four different expeditions, including the Arctic Summer Cloud Ocean Study (ASCOS; www.ascos.se, also see Tjernström et al., 2013) revealed a neutrally stratified layer extending from the surface up to about 300–600 m (Tjernström et al., 2012), which indicates that the surface and the boundary-layer clouds could potentially be thermodynamically connected. Shupe et al. (2013) investigated the interactions between the cloud and boundary layer using one week of observations from ASCOS and found, however, that for this time period, such coupling took place only 25 % of the time; the rest of the time the cloud layer was decoupled from the surface. In addition, even when clouds were connected to the surface, the surface fluxes did not seem to drive this coupling; instead they simply responded to the mixed-layer processes aloft, driven primarily by in-cloud generated turbulence.

The present study is also based on ASCOS data and provides a complementary view on cloud-surface interactions to that by Shupe et al. (2013). They used profiles of turbulence dissipation rate ε, derived from Doppler radar velocities, to determine the depth of the cloud-driven mixed layer below cloud base and thus the state of cloud-surface coupling. Here we instead use vertical profiles of equivalent potential temperature, $\Theta_E = \Theta(1 + LQ_v/C_pT)$, a conserved quantity during moist adiabatic processes, to identify stability and stability changes within the cloud and sub-cloud layers. While deriving profiles of ε from the cloud radar requires more ideal conditions than observing the thermal structure of the lowest troposphere, our method allows us to examine

ACPD
14, 3815–3874, 2014

profiles from all periods (Tjernström et al., 2013) of ASCOS, from the ice-drift as well as the transit periods (to/from the ice-drift); this has allowed us to include substantially more data in our analysis, compared to the week-long period characterized by relatively steady conditions and free-atmosphere subsidence. The present study is organized as follows; Sect. 2 includes a brief description of ASCOS, the atmospheric conditions and the instrumentation deployed; included here is also a discussion on the analysis methods. Section 3 describes the results of this study while a discussion and conclusions are given in Sects. 4 and 5 respectively.

2 Data and methods

2.1 ASCOS

ASCOS operated under the fourth International Polar Year (IPY 2007–2009) and was an intensive field experiment observing many aspects of the atmosphere, sea ice and the upper ocean for 40 days through August and late September 2008, in the North Atlantic sector of the central Arctic Ocean (~ 87.5° N). Tjernström et al. (2013) provides a detailed description of this endeavor, as well as of the instruments and measurement strategies that were deployed. ASCOS was conducted on the Swedish ice-breaker *Oden*, which left Longyearbyen on Svalbard on 2 August (Day of Year; DoY 215) and returned on 9 September (DoY 253). Between 12 August (DoY 225) and 2 September (DoY 246), *Oden* moored and drifted with a 3 × 6 km ice-floe where an ice camp was established. The drift track was approximately from 87°21′ N 01°29′ W to 87°09′ N 11°01′ W; this period will be referred to as the "ice drift", see Tjernström et al. (2013) for details.

One of the aims of the expedition was to study the formation and life-cycle of low-level clouds, with a focus to better understand their impact on the surface energy budget, especially during the fall transition towards sea-ice freeze up. Detailed observations of Arctic clouds are sparse, limited in time and space to a small number of intensive

ACPD
14, 3815–3874, 2014

observational campaigns, including SHEBA (Uttal et al., 2002) and AOE-2001 (Leck at al., 2004; Tjernström et al., 2004) or the pan-Arctic observatories discussed in Shupe et al. (2011). ASCOS included arguably the most comprehensive suite of instruments for observing surface, atmospheric and cloud processes over a remote sea-ice environment (Tjernström et al., 2013).

Large-scale atmospheric conditions during ASCOS are documented in Tjernström et al. (2012) while detailed descriptions of the meteorological conditions encountered during ASCOS ice drift are provided by Sedlar et al. (2011) and Tjernström et al. (2012, 2013); hence only a brief recap will be provided here. Sedlar et al. (2011) analyzed the surface energy budget during the ice drift and defined four main periods with different energy budget and cloud characteristics. Tjernström et al. (2012) also took the surface temperature variability and vertical structure of the lower troposphere into account and divided their first period into two sub-periods, defining five different periods in total. These are the periods we adapt here, in addition to the transit periods before and after the ice drift, in and out of the pack ice. The 5 ice drift periods are shown in Fig. 1, overlaid on the reflectivity from the vertically pointing cloud radar; DoYs prior to 226 and after 246 are during the transit towards and away from the ice drift, respectively.

The first (DoY 226–230) and second (DoY 230–234) periods during the ice drift had the largest positive surface energy residuals, indicating melt was still ongoing (Sedlar et al., 2011). Surface temperatures were mostly close to the melting point of fresh water during these periods. Both periods were affected by synoptic weather systems and deep frontal cloud structures, but the first was synoptically more active (Fig. 1) and significantly more variable in temperature than the second. This period of synoptic activity ended on the evening of DoY 233. During the third period (DoY 234–236) a sharp drop in temperature was observed, down to −6 °C. Quiescent conditions prevailed during these two days and an intermittent, and occasionally tenuous, low-level stratiform cloud or fog layer emerged below an upper level optically thin cirrus layer (Sedlar et al., 2011). On DoY 236, another frontal system passed overhead resulting in heavy snow fall during much of the evening. After that, the following 4th period (DoY 236–244) was

ACPD
14, 3815–3874, 2014

characterized by high pressure and large-scale subsidence in the free troposphere with only weak frontal passages. Single and multi-layered stratiform clouds below 2 km were persistent for nearly the entire week (Sedlar et al., 2011), with relatively thin liquid cloud layers and ice crystals growing within, and falling from, these layers. The surface temperatures were somewhat higher, close to the freezing point of ocean water, but still below fresh-water melting. Sedlar et al. (2011) concluded that this period was vital to the transition of the surface towards the seasonal freeze up. These relatively steady conditions continued during the 5th period (DoY 244–246), when an area with partly clear skies and optically thin clouds was advected over the ASCOS site, allowing surface temperatures to plummet below −12 °C and the autumn freeze-up to initiate (Sedlar et al., 2011). Finally, during both transit periods, before and after the ice drift, numerous synoptic weather systems were encountered; see Tjernström et al. (2012) for detailed profiles of radar reflectivity and subjective analysis of frontal profiles during each of these periods.

2.2 Instrumentation

A detailed description of all ASCOS instrumentation is provided by Tjernström et al. (2013). Here, only basic information about the instruments used in this study is given, while further details can be found in the cited references.

Information on the vertical atmospheric structure is derived from radiosondes and a 60 GHz scanning radiometer. Radiosoundings were released approximately every 6 h. Although the limited temporal resolution is a major disadvantage, radiosondes provide accurate temperature, moisture and wind measurements. The scanning radiometer (Westwater et al., 1999) provides temperature profiles up to 1200 m with a vertical resolution of around 7 m near the surface, gradually deteriorating with altitude to about 200 m at 1 km. A 5 min averaging window was applied to the 1 Hz raw data to improve the signal-to-noise ratio. The scanning radiometer has been shown to provide accurate measurements, with a low root mean square error relative to independent radiosondes up to 800 m (P.O.G. Persson, personal communication, 2013); above this height, the

ACPD
14, 3815–3874, 2014

scanning radiometer temperatures gradually revert to the linear interpolation between the radiosonde profiles used as the a priori assumption in the retrieval process. Nevertheless, due to its high temporal resolution, and the fact that many of the cloud and sub-cloud layers are contained below 800 m, these profiles provide a valuable coherent data set of temperature profiles.

Cloud boundaries and characteristics are derived from a vertically-pointing 35 GHz Doppler Millimeter Cloud Radar (MMCR; Moran et al., 1998). The vertical resolution is 45 m with a lowest radar gate of 105 m and a time resolution of 10 s. The measured Doppler spectrum was processed to estimate the three Doppler radar moments: radar reflectivity (dBZ), mean Doppler velocity ($m\,s^{-1}$) and Doppler spectrum width ($m\,s^{-1}$) in clouds and precipitation. The reflectivity, which is nominally proportional to hydrometeor size to the sixth power, is usually dominated by ice crystals since they are normally larger than liquid droplets. The fall velocity of the hydrometeors can also be used to assist in distinguishing hydrometeor phase; cloud droplets have a very small, nearly negligible, fall velocity, whereas ice crystals and drizzle/rain droplets generally fall with larger velocities. As is common in vertically-pointing radar meteorology, a positive Doppler velocity is defined downward. Moreover, the Doppler spectrum width can provide indications of multiple cloud phases, i.e., particles in the same volume with different fall speeds, and/or turbulence within the radar pulse volume. Under most observed conditions, the MMCR can accurately identify cloud top; however when precipitation occurs between multi-layer clouds, the MMCR may not provide information on cloud top height for lower layers. The full Doppler spectra were used to create spectrographs of vertically-resolved reflected power as a function of Doppler velocity. These proved useful for distinguishing multiple cloud layers when other sensors indicated the potential for cloud layering masked by precipitation; spectrographs are discussed in Sect. 2.3.

MMCR derived cloud boundaries are also complemented with additional remote sensors. Cloud base is derived using two laser ceilometers with a sampling interval of 15 s. In general, laser ceilometers become attenuated by large concentrations of liquid

ACPD
14, 3815–3874, 2014

droplets; this instrument is therefore able to penetrate precipitating layers of ice crystals and drizzle droplets and identify the vertical locations of up to 3 cloud bases, provided the lower cloud layers are not too optically thick. Once the return signal is attenuated, it is not possible to detect additional cloud layers aloft. A comparison of the two time series revealed relatively good agreement between the two instruments.

A dual-channel microwave radiometer provides vertically-integrated liquid water path (LWP) retrievals with an uncertainty of 25 g m^{-2} (Westwater et al., 2001); ice water path (IWP) is estimated using a multi-sensor cloud phase classification and MMCR reflectivity power–law relationships (Shupe et al., 2005). Cloud condensation nuclei (CCN) concentration was measured by an in situ CCN counter (Roberts and Nenes, 2005), set at a constant supersaturation of 0.2 %, based on typical values used in other similar expeditions (Bigg and Leck, 2001; Leck et al., 2002). These CCN measurements were made on the ship via an inlet at 25 m above the surface.

Finally, turbulent fluxes are derived using two techniques. Eddy covariance measurements are available from the ice drift (12 August–1 September) at heights between the surface and 30 m from sensors deployed on two masts on the ice. The uncertainty of individual turbulent flux estimates is not easy to determine but is generally considered to be around 10 % (Andreas et al., 2005). Diffusional and rime icing on the turbulent flux instrumentation poses a more critical problem, which leads to time periods when turbulent fluxes could not be estimated. To maximize the use of this data, a single consensus time series was created from all available data, regardless of height, assuming it was all sampled within the so-called "constant-flux layer"; tests indicate that this is a reasonable approximation.

So-called "bulk turbulent fluxes", based on the mean vertical differences, are less accurate than direct measurements but data from instruments onboard the ship allow fluxes to be estimated for the whole expedition. Static stability is estimated from the Marine Atmospheric Emitted Radiance Interferometer (MAERI) instrument onboard *Oden* to fill missing data periods from the eddy correlation measurements, as well as to extend the observations of turbulent fluxes to the entire ASCOS expedition. MAERI

ACPD
14, 3815–3874, 2014

measured air temperature, viewing horizontally out from its position at 21 m on the port side of the ship, and the surface temperature, viewing down at the surface from the same position. These data were combined with the observed humidity, assuming a saturated surface with respect to the observed temperature, and wind speed from the ship's weather station to obtain the turbulent fluxes using the TOGA COARE bulk flux scheme, modified for Arctic sea-ice conditions (Persson et al., 2002). However, MAERI temperatures were sometimes affected by certain physical factors; when the ship was oriented so that the MAERI sensor viewed open ocean, rather than ice, it sometimes measured a higher temperature than over the adjacent ice surface, leading to an overestimation of the heat fluxes. Also, when the wind direction was from *Oden's* starboard side, the MAERI, located on the port side, may have observed too high air temperatures due to the heat plume from the ship; then the sensible heat flux is likely underestimated.

2.3 Analysis method

The first MMCR range gate in the vertical with a return power below the radar sensitivity demarcates the cloud top, while the highest observed ceilometer cloud base below cloud top is considered as the base for this layer. Both ceilometers are used for consensus. Median cloud boundaries were computed from a 2 min window following each scanning radiometer measurement and a 10 min window following each radiosonde release. For the analysis of cloud bulk properties (LWP, IWP) and the radar Doppler moments, the same time windows were used to derive median values. Considering the persistence of low-level Arctic clouds (Shupe et al., 2011), the assumption that the median cloud layers are in steady state over the above applied time-windows is reasonable. The analysis of the median boundaries is used instead of the mean, in order to reduce the effect of outliers (Sedlar et al., 2011), as may occasionally occur with only slightly less than complete overcast conditions or when a second cloud layer emerges within the time window following thermodynamic profiles.

ACPD
14, 3815–3874, 2014

Profiles of Θ_E are used to define the cloud-driven turbulent mixed layer; depending on whether this layer extends until the surface or not, the cloud is classified as either "coupled" or "decoupled", respectively. If a cloud-driven mixed layer is not observed, then the cloud is classified as "stably-stratified". Note that "stably-stratified" clouds are also not connected to the surface, but here with the word "decoupled" we refer only to cases with a cloud-driven mixed layer diagnosed. Two sets of data are used; either directly using the radiosoundings or combining the scanning radiometer temperature profiles with interpolated specific humidity from the soundings. While the radiosonde equivalent potential temperature data is more accurate, it also has temporal limitations. On the other hand, while the interpolation of specific humidity is a limitation for the scanning radiometer data, it allows using the higher temporal resolution to enhance the number of profiles that could be included in the study. The classification of the vertical structure of the clouds based on the scanning radiometer profiles is in good agreement with the results derived from the radiosonde dataset. Therefore, the majority of the results in this study are based on the scanning radiometer, while for other information the radiosonde data is used (e.g., humidity and wind).

An algorithm was developed to identify the main temperature inversion in the layer extending above cloud base until 100 m above cloud top, by applying thresholds to the Θ_E profiles. A quasi-constant Θ_E from the inversion base down to the surface is taken to indicate coupling, whereas a decrease towards the surface below the cloud indicates a local stable layer and hence decoupling. The height at which the Θ_E has decreased by 0.5 °C, compared to the cumulative mean value of the layer above, is considered to be the decoupling height. This threshold was selected to optimize between accuracy and reliability, given the vertical variability of the observed temperature especially in the soundings, and the results are reasonably insensitive to small changes in the threshold. The layer between the cloud base and the decoupling height will be referred as the sub-cloud mixed layer (SML). Both coupled and decoupled clouds will be often referred as neutrally-stratified clouds, referring to the gradient Θ_E profile within the cloud layer. If the gradient of Θ_E is positive through the whole cloud layer, it is classified as a stably-

ACPD
14, 3815–3874, 2014

stratified or stable cloud. Moreover, profiles where an inversion near cloud top could not be identified were reexamined by estimating the Θ_E gradient from cloud top to cloud base. These profiles were found to have large gradients and so these cases are also considered to be stable clouds. To illustrate qualitatively the differentiation of the categories using the Θ_E profiles, examples are given in Fig. 2 for coupled (Fig. 2a), decoupled (Fig. 2b) and stable clouds with a main inversion identified close to the cloud top (Fig. 2c) and with no main inversion identified (Fig. 2d).

Only profiles with a cloud top below 1500 m, a cloud base below 1200 m and a cloud thickness larger than 135 m (three radar gates) are included in the analysis. In addition, profiles where cloud thickness is greater than 700 m are assumed to be two cloud layers with precipitation falling from the upper cloud and where the ceilometer fails to penetrate the lower cloud to detect the upper cloud base. For some of these cases, it is possible to estimate the upper cloud base from spectrographs. Two examples are shown in Fig. 3. For these cases, the first record of the MMCR radar is the top of the upper cloud, whereas the existence of a lower dense cloud or precipitation prevents the ceilometer from measuring the corresponding cloud base. In these cases the cloud top and base derived directly from the instruments is 960 m and 90 m, and 1095 m and 75 m, respectively, but from the spectrographs we could infer that the base of the upper cloud is around 750 m and 700 m, respectively. These are the levels where the Doppler velocities become systematically large and positive, indicating falling hydrometeors and no longer contained within the liquid cloud layer, using the assumption that cloud droplets are small and have negligible (near 0 m s^{-1}) fall velocities. Hence the height where significant radar power crosses the zero velocity line is indicative of the liquid base height.

When using radiosonde profiles for the classification, the same cloud thickness criteria are applied, but using a less strict cloud top criterion, including cloud returns 3000 m (rather than 1500 m for the scanning radiometer profiles). The stricter cloud boundary criteria used for the scanning radiometer are necessary due to the limited vertical extent of the measurements that this instrument provides. The less strict cloud-

ACPD
14, 3815–3874, 2014

top criterion for the radiosonde profiles is chosen because of the shorter time-series that this instrument provides and the need to include as many profiles as possible in our analysis.

Applying the above criteria, 3436 out of the total available 8261 scanning radiometer profiles are considered, or 42 %. For almost 40 % of the available ASCOS profiles, a proper low cloud top, as defined above, was not detected by the radar due to the presence of deep precipitating weather systems (see Fig. 1), whereas around 18 % fail to pass the geometrical restrictions. Hence, considering only the times when deep weather systems were not present, the algorithms described above capture roughly two thirds of the available data. As a comparison, 87 out of the 145 radiosonde profiles pass the above criteria for similar reasons.

To investigate the liquid and ice water cloud properties that characterize each cloud state, single cloud-layer profiles had to be selected, since the derived LWP is a vertically-integrated quantity; the vertical distribution of the liquid is unknown, and with multiple cloud layers it becomes impossible to partition the liquid among layers. For this particular purpose, profiles where the ceilometer detected more than one cloud base or the MMCR detected more than one cloud top were rejected. Out of the 3436 scanning radiometer profiles that are used for the main analysis, slightly less than half, or 1611, represent single cloud layers and are used for the analysis of cloud liquid and ice characteristics.

3 Results

3.1 Cloud states

Considering results based on the scanning radiometer alone, 40 % of the cases are decoupled while 28 % are coupled and 32 % are considered stable (Fig. 4, dark blue). The corresponding results from the radiosonde profiles are 46 % decoupled, 23 % coupled and 31 % stable. The somewhat higher (lower) fraction of decoupled (coupled) clouds

ACPD
14, 3815–3874, 2014

for the radiosondes may be due to the inclusion of higher cloud tops; as will be shown later, higher clouds are more likely to be decoupled than lower ones. Considering the limited number of soundings available, the agreement is reasonable and supports the use of the scanning radiometer profiles for the analysis.

The relative frequency distribution (RFD) of coupled, decoupled and stable cloud profiles derived either from the scanning radiometer (Fig. 4) or the radiosonde (not shown) reveals that neutrally-stratified clouds (coupled plus decoupled) are more frequent during ASCOS than stable clouds. Yet, in the majority of the neutral cloud cases the cloud-generated turbulence does not mix with the boundary layer below down to the surface and the cloud remains decoupled. Included in Fig. 4 are the RFDs of coupled, decoupled and stable clouds for each period of ASCOS (see Sect. 2.1). Many deep precipitating weather systems advected overhead from the beginning of the expedition until the end of the 2nd ice-drift period, and during the transition to the end of ASCOS (Fig. 1). Hence there were only short and scattered occurrences of low stratocumulus during these periods, which is why few profiles are included here.

From the beginning of ASCOS until the end of the 2nd period of the ice drift, stable and coupled clouds dominate; nearly 80 % of the profiles satisfying the geometric cloud constraints described above during DoY 216–230 contain low clouds with tops below 500 m. The high fraction of stable clouds during this time is likely due to optically (and geometrically) thin clouds, presumably with insufficient liquid water to drive in-cloud mixing strong enough to overcome the boundary layer stability or the effects of advection; this will be investigated below. In the cases where a cloud-driven mixed layer is observed, the proximity of these clouds to the surface makes it easier for the cloud-generated motions to interact with surface-generated turbulence (Shupe et al., 2013), which we speculate is the reason why decoupled cases are rare during these early periods of ASCOS.

During the second period of the ice drift (DoY 230–234), higher clouds with tops above 800 m between the deeper precipitating systems are observed, which are either decoupled or stable; however the later is still the dominant state. During the third period

ACPD
14, 3815–3874, 2014

of the ice drift (DoY 234–236), coupled and stable cases are the only states observed, but now with coupled being the most frequent. This period is dominated either by very low clouds or fog (95 % of the profiles have a cloud top below 400 m).

The fourth period of the ice-drift (DoY 236–244) provides almost half of the profiles included in this study. This is the longest period and also the one that was examined by Shupe et al. (2013) and Sedlar and Shupe (2013) to study the cloud-surface interactions and vertical velocity characteristics during ASCOS. The persistent stratiform layer (Fig. 1) is often decoupled but intermittently connects thermodynamically with the surface. Stable clouds are observed in only ∼ 10 % of these profiles. Taking only the neutrally-stratified profiles into account, 74 % are found to be decoupled and 26 % coupled; this is in very good agreement with the occurrence statistics found in Shupe et al. (2013) and Sedlar and Shupe (2013).

During the fifth period (DoY 244–246), neutrally-stratified clouds still dominate, although a considerable portion (∼ 35 %) of stable cases are also observed. At the beginning of this period the stratiform cloud conditions from the previous period persists, but are gradually decreasing in depth and height, and becomes tenuous, and at some points even dissipates (Fig. 1). Finally, from the transit period away from the ice drift, few profiles are included because of the occurrence of several deep precipitating weather systems. Most profiles are derived from DoY 246–248, when a low stratiform cloud layer is observed, and from a few hours during DoY 249 and 251, when a very low tenuous cloud is apparent in the MMCR reflectivity (Fig. 1).

The RFDs for cloud boundaries and cloud thickness are shown in Fig. 5. The distribution of cloud top indicates that decoupled clouds have higher tops than the coupled and stable clouds (Fig. 5a). The distributions for coupled and stable cases have peaks between 300–500 m, with a long tail extending to higher values, whereas the peak for decoupled clouds is around 900–1100 m with a long tail towards lower top heights. In general, clouds with tops above ∼ 900 m are usually decoupled while those with tops below ∼ 500 m are coupled or stable. The frequency distribution for cloud base (Fig. 5b) shows that coupled and stable clouds have a cloud base below ∼ 200 m during more

ACPD
14, 3815–3874, 2014

than 50 % of their occurrences, whereas the decoupled cloud base distribution peak is much broader between 400 and 800 m. In addition, the RFD for cloud thickness (Fig. 5c) indicates that stable clouds are geometrically thinner than neutrally-stratified clouds, whereas decoupled clouds are in general no thicker than the coupled clouds.

In summary, this analysis shows that stable clouds are geometrically thin and low, while neutrally-stratified clouds are thicker and found higher above the surface. However, decoupled clouds appear higher up in the atmosphere than coupled clouds; neutrally-stratified clouds seem connected to the surface boundary layer when cloud top is below ~ 700 m and remain decoupled when it is above ~ 900 m. These results provide hints at the mechanism explaining the different cloud classes. While turbulence is practically always generated at the surface by mechanical mixing, unless very weak winds prevail, strong radiative cooling at cloud top normally gives rise to buoyancy-generated turbulence inside the cloud layer. In cases when the cloud layer is sufficiently close to the surface, the two layers can connect, leading to a continuously coupled state. On the other hand, when cloud layers are displaced higher, with cloud tops above 700 m, the in-cloud turbulence generated at the cloud top usually does not penetrate to the surface-based mixed layer and thus becomes independent of the surface conditions; the cloud state is decoupled. An exception to this description is a number of low clouds that are not mixed at all (stable cloud states); these are about half of the lowest and thinnest clouds, with cloud bases < ~ 200 m and thicknesses < ~ 300 m. This indicates that these thin clouds do not cool sufficiently to space at the top, probably because they are either too optically thin or the liquid water content is distributed rather homogenously across the cloud layer, but also that the surface generated turbulence is often too weak to mix clouds even when they lie below a few hundred meters.

The mixed layer of the decoupled clouds is explored further in Figs. 6 and 7. Decoupling heights are typically low, 50–400 m (Fig. 6a), while decoupling above 600 m rarely occurs. For 70 % of the cases, the cloud-generated turbulence extends to 200–600 m below cloud base (Fig. 6b). Different distribution shapes in Fig. 6a and b suggest that the cloud-generated mixing depth below base depends on the cloud base height. The

ACPD
14, 3815–3874, 2014

relationship between cloud boundaries and the depth of the SML is shown in Fig. 7. In general, the depth of the SML increases as cloud base and top heights increase (Fig. 7a and b). Yet, SML depths are almost indifferent to cloud thickness and increase only slightly with increasing cloud thickness (Fig. 7c). However, it must be recalled that the range of thickness is similar for nearly all low-level cloud mixing states (see Fig. 5c). The above general relationships were also observed by Shupe et al. (2013), although for a shorter period.

3.2 Surface fluxes

To examine the influence of the turbulent surfaces fluxes on the cloud coupling state, RFDs of momentum, sensible and latent heat fluxes for the three cloud coupling states are shown in Fig. 8. Two turbulent flux data sets are used here: direct eddy correlation measurements from the ice drift only, and bulk fluxes for the whole experiment. Upward heat fluxes are positive for the surface losing heat to the atmosphere whereas momentum flux is a scaled parameter, thus always positive. Turbulent heat fluxes are generally very small while the momentum fluxes can be substantial (Tjernström et al., 2012). A comparison of the two time series during times when they overlap (not shown) revealed relatively good agreement for the momentum and sensible heat fluxes, whereas the latent heat fluxes exhibited larger differences; see Sect. 2.2 for a discussion.

RFDs for momentum flux (Fig. 8a) show no significant difference among the three cloud states, although decoupled state has a broader peak over slightly higher values. This is contrary to expectations; a larger momentum flux means more mixing and, if it was important for the cloud state, less likely to be present in a decoupled state. These distributions indicate that mechanical mixing is not a leading factor that determines coupling state. The same conclusion holds for the sensible (Fig. 8b) and latent (Fig. 8c) heat fluxes, suggesting that surface turbulence is not responsible for cloud-surface coupling states and that these interactions are thus mainly driven by the cloud. This is in agreement with the results from Shupe et al. (2013).

ACPD
14, 3815–3874, 2014

3.3 Cloud water properties

Cloud water properties are analyzed from single cloud-layer cases only; see Sect. 2.3. This further reduces the number of profiles by about 50 %. Of these 52 % were decoupled, 31 % coupled and 17 % were stable. The lower fraction of stable cases suggests that these are often secondary clouds. However, the ratio between the two mixing states compares favorably to the results from the whole period and those from only soundings.

The results in Fig. 9a are shown as box-and-whisker plots, and in Fig. 9b as histograms; the notched boxplots highlight the significance of any statistical difference between the medians of different samples at approximately 95 % confidence level, whereas the histogram offers a more detailed view of the results. Negative (unphysical) LWP values included in the statistics are due to the LWP uncertainty of $\sim 25\,\mathrm{g\,m^{-2}}$ from the MWR instrument. Figure 9a reveals that the stably-stratified cloud state is statistically different from neutrally-stratified cloud states, since the LWP median ($\sim 32\,\mathrm{g\,m^{-2}}$) is significantly smaller than the corresponding values for the latter states (64–65 $\mathrm{g\,m^{-2}}$). This confirms the initial hypothesis about the origin of the stable cases; a cloud emits radiation as a blackbody when LWP reaches $\sim$ 30–50 $\mathrm{g\,m^{-2}}$ or higher (Stephens, 1978). Cloud LWPs for the stable state are often at or below this blackbody emission range, and it is likely that cloud-top radiative cooling and buoyant mixing are reduced. The two neutrally-stratified cloud states exhibit no statistical difference, suggesting that transitions from a coupling to a decoupling state (and vice versa) are not driven by changes in LWP.

Histograms of LWP for the three cloud types (Fig. 9b) also indicates that the stable cloud state in most cases are optically thin; for 72 % of the stable cloud profiles the LWP is below 50 $\mathrm{g\,m^{-2}}$. Note, however, that even if the bulk of a cloud contains enough liquid to be "blackbody", as manifested by the LWP, the buoyancy-generation of turbulence depends on the differential cooling in the vertical. Thus, in a cloud with marginally LWP, the layer affected by longwave cooling may become too thick in relation to the cloud

ACPD
14, 3815–3874, 2014

thickness and instead of generating turbulence and mixing the whole cloud layer will cool. The RFDs for both neutrally-stratified states have peaks between 50–80 $g\,m^{-2}$, although the decoupled clouds have their peak shifted slightly to higher values compared to the coupled clouds. This result disagrees with Shupe et al. (2013), who found that coupled clouds tend to have more LWP than decoupled. The difference in results is presumably related to different methods (thermodynamic vs. dynamic) to determine the mixing states of the clouds and that the present study includes a longer time series of data spanning a larger variability in large-scale meteorological conditions.

To investigate how the choice of a certain period of data affects the statistical results, we also calculated the statistics of LWP for the 4th period of ASCOS ice drift separately, which was analyzed by Shupe et al. (2013), and compared them to the remaining periods. Considering only the 4th period, the median LWP for coupled clouds is $\sim 77\,g\,m^{-2}$ and its 25th percentile is $\sim 58\,g\,m^{-2}$, while for the remaining periods it is ~ 58 and $\sim 43\,g\,m^{-2}$, respectively (not shown). This comparison shows that coupled cases during a persistent and relatively thick stratocumulus deck (Fig. 1) contained relatively more liquid than during the other periods, indicating that part of the difference lies in the differing time samples. This illustrates the importance of having long time series for this type of analysis.

The results for the IWP (Fig. 10) also show significant difference between the stable clouds and the other two cloud types; stable cloud states have an IWP median around $\sim 0.5\,g\,m^{-2}$, which is 4–6 times smaller than that for the neutrally-stratified cloud states, and frequently has zero IWP. The medians for the coupled and decoupled states are around ~ 3.2 and $\sim 2.7\,g\,m^{-2}$, respectively. All RFDs have a large tail towards larger IWP values. The fact that stable cases have IWP close to zero indicates that these clouds are often not mixed-phase. Furthermore, some of these stable clouds with a relatively low LWP and little/or no ice, are probably cases of fog, which agrees with their lower cloud boundary statistics described above.

ACPD
14, 3815–3874, 2014

3.4 CCN concentrations

Figure 11 illustrates near-surface CCN concentrations observed during coupled, decoupled and stable states. The available CCN data corresponds to the period between DoY 228–252, while during that time there are several short periods where no data are available at all (e.g., due to pollution contamination by ship exhaust; see Martin et al., 2011). As a result, it is possible to match a CCN concentration to a cloud state for only 25 % of the total scanning radiometer profiles.

The median CCN concentration (Fig. 11) for stably-stratified clouds is $\sim 21\,\mathrm{cm}^{-3}$, whereas for neutrally-stratified cases the medians are twice as large, ~ 43–$44\,\mathrm{cm}^{-3}$. The low CCN concentrations explain the limited ice and liquid amounts present in stable clouds; the low number of activated liquid droplets reduces the possibility of droplet evaporation to sustain vapor deposition to ice in a saturated environment, so that these few droplets eventually grow larger and larger, until they fall out under gravity (e.g., Mauritsen et al., 2011). Thus, low CCN concentration for the stable cases is additionally support the hypothesis that stable clouds are optically thin.

3.5 Vertical structure

To investigate the structure and phase of the clouds, RFDs of radar reflectivity as a function of height are shown in Fig. 12. These results are shown on a scaled vertical axis, slightly different for the three different cloud states. For coupled clouds, $z_n = -1$ represents the vertical level of the MMCR's first range gate, $z_n = 0$ is the cloud base and $z_n = 1$ the inversion base. Stable cases are normalized in similar manner, except that $z_n = 1$ is at the cloud top, since a temperature inversion associated with the cloud top is not always present; note that reflectivity above the cloud top are present in Fig. 12c, as a stricter definition on radar reflectivity was used here to identify cloud boundaries, while the full reflectivity profile was used for the statistics. Decoupled clouds have three layers and hence the surface is at $z_n = -2$ while $z_n = -1$ is the decoupling height, $z_n = 0$ the cloud base and $z_n = 1$ the inversion base. Heights above $z_n = 1$ (the free tro-

ACPD
14, 3815–3874, 2014

posphere) are also scaled by the thickness of the layer below, since there is no other obvious scaling.

For coupled clouds (Fig. 12a) the range of reflectivity values extends from −35 dBZ to −5 dBZ, with a maximum frequency around −20 dBZ, throughout the whole cloud, and almost the whole sub-cloud layer although the spread is larger here. A rapid decrease is only observed close to the surface, where evaporation or sublimation of precipitation takes place. Above the inversion base, the maximum RFD remains constant to about $z_n \approx 1.3$, suggesting that the top of these clouds usually extend into the inversion layer (e.g., Sedlar et al., 2012). The median profile's behavior is similar to the RFDs structure but is consistently higher, indicating a positively skewed reflectivity distribution.

The stable cases (Fig. 12c) are generally characterized by lower reflectivity compared to the coupled cases. In the lower half of the cloud, reflectivity extends between −50 dBZ and −15 dBZ, with a maximum frequency around −40 to −30 dBZ. Below cloud base, the decrease in magnitude with decreasing height is more pronounced than for coupled cases; the reflectivity is reduced by ∼ 10 dBZ already at $z_n \approx -0.3$, although the width of the distribution increases, explaining the more gradual change in the median. In the upper half of the cloud, reflectivity decreases rapidly with height. The in-cloud reflectivity values are often well below −17 dBZ, a general upper limit of cloud droplet only returns (Frisch et al., 1995), supporting the notion of stable clouds containing very small concentrations of precipitation-sized hydrometeors.

Decoupled clouds (Fig. 12b) have a similar structure to the coupled cases inside the cloud, but exhibit a larger spread in reflectivity values below cloud base. The reflectivities of the layer between inversion base and cloud base extend from −40 dBZ to −5 dBZ, whereas the values of the sub-cloud layer show an even larger spread especially towards the smaller values (down to −65 dBZ). The depth of the SML often varies between 200–600 m (Fig. 6). Thus, larger variability in the sub-cloud layer reflectivity (Fig. 12b) may be due to different features or characteristics of the decoupled cloud and/or sub-cloud layers depending upon SML depth.

ACPD
14, 3815–3874, 2014

In an attempt to investigate how the depth of the decoupled sub-cloud layer affects the vertical structure of precipitation, we use the relationships between the three radar moments at the decoupling height and the depth of the SML (Fig. 13). Figure 13a reveals that reflectivity at the decoupling height decreases gradually as the mixed layer deepens. For depths greater than 500 m, a distinct peak in the RFD is apparent for very small reflectivities (< −50 dBZ). Likewise, the RFD of Doppler spectrum width (Fig. 13c) also shows a decrease in Doppler velocity variance for SML depths > ∼ 300 m. Combined, these results suggest that precipitation intensity within the volume near the decoupling height tends to be larger when the mixed layer depth is shallower. However, the mean Doppler velocity distribution (Fig. 13b) at the decoupling height shows a slight tendency to increase for SML > ∼ 400 m. This result appears to be inconsistent with the other two radar moment distributions with SML depth, as decreasing reflectivity and reduced spectrum width tend to suggest a more homogeneous hydrometeor distribution of generally smaller sizes. One possible explanation is that as precipitation falls through a deeper SML, smaller hydrometeors evaporate faster while larger crystals continue to fall with large velocities (Fig. 12b); the deeper SML depths also means a longer fall duration of precipitation through the sub-cloud layer, potentially increasing the amount of sublimation of the smallest ice crystals. This lower concentration of precipitation is reflected in both Figs. 12a and c. Nevertheless, all radar moments show a bimodality in RFD for the primary SML depths observed. To get a clearer distinction of the conditions that drive the decoupling at different depths, we separate the decoupled clouds in two sub-categories: those with a SML depth less than 450 m and those with a SML deeper than 500 m; 60 % and 30 % of the total decoupled profiles respectively. Thus clouds with a shallower SML occur twice as often. The first category includes the lower decoupled clouds, whereas the latter includes some of the highest clouds observed (see Fig. 7a).

In Fig. 14, the reflectivity for decoupled clouds is shown again, but now divided into the two categories. The decoupled clouds with the shallower SML (Fig. 14a) have a very similar structure to the coupled clouds (Fig. 12a). The range of reflectivity values

ACPD
14, 3815–3874, 2014

from inversion base to cloud base is about the same and remains constant throughout the SML. On the other hand, decoupled clouds with a deeper mixed layer (Fig. 14b) largely differ from all the other cases: the maximum occurrence frequency close to the inversion base is around −20 dBZ, same as for the coupled and decoupled clouds with shallow SML, but near cloud base it decreases to −30 dBZ. This is the only case where a decrease inside the cloud layer is observed, suggesting that these clouds have little ice, such that the reflectivity profile within the cloud is actually dominated by the liquid water. Furthermore, in the sub-cloud layer, reflectivity distribution is bimodal and has two completely different structures. In some cases the reflectivity remains constant through cloud and upper sub-cloud layers very similar to coupled and decoupled cases with a shallower SML; this branch in the RFD however decreases and vanishes closer to the surface. The lack of values below the decoupling height suggests that these profiles get decoupled around 100 m, the lowest vertical range gate of the MMCR; this shallow decoupling agrees with the RFDs of decoupling height (Fig. 6a), where ∼ 40 % of the decoupling heights were found below 200 m. For the other mode, there is also a decrease with decreasing height, from values < −40 dBZ below cloud base until the decoupling height where the reflectivity minimum is reached, approaching −60 dBZ. This illustrates the large potential impact on hydrometeors that evaporation/sublimation may have, when precipitation falls through a relatively deep sub-saturated layer.

Next the thermodynamic structures of the different (now four) cloud states are analyzed. We did not find any relationship between cloud states and either cloud top, cloud base or surface temperatures (not shown), so only the gradients of potential temperature profiles are shown in Fig. 15. Note, these are gradients of Θ profiles and not Θ_E,on which the separation of coupled, decoupled and stable state was based. Through the definition of Θ_E, an increase in Θ across a layer could be compensated by a decrease in Q_v leading to a constant Θ_E; hence, a thermodynamically coupled case as defined here using Θ_E could appear decoupled when using the Θ profile. Figure 15, showing the statistics of the Θ gradient profiles with respect to normalized height (same as for radar reflectivity), reveals that this does not occur here.

ACPD
14, 3815–3874, 2014

In coupled cases (Fig. 15a), the Θ gradient is slightly larger than zero in the cloud, consistent with the release of latent heat in the cloud interior, and remains almost constantly near-zero in the sub-cloud layer until the surface, where it slightly increases. In both the decoupled classes, two separate layers below the cloud base are apparent. For the shallow SML (Fig. 15b) category, Θ gradient is near-zero from inversion base until the decoupling height, followed by a weak second inversion around the decoupling height and slightly stronger stability below. Near the surface, the Θ gradient goes to near-zero or even slightly negative, suggesting the existence of a turbulent surface-layer. The secondary inversion is much more pronounced for the decoupled state with a deeper SML (Fig. 15c). Here the layer above the decoupling height is also substantially less stable compared to the layer below. This difference in thermal structure explains separation between decoupled cloud states with shallower or deeper SML; it actually is a separation between states that are "weakly decoupled" or "strongly decoupled". Thus from here and onwards we will examine four cloud states, using the "weakly" and "strongly" decoupled terminology, rather than "shallow" or "deep". In most stable cases (Fig. 15d), the near-surface structure is somewhat more neutrally stratified. The stratification is strongly stable throughout the profile and these clouds are disconnected from surface sources.

Figures 16 and 17 show normalized profile RFDs of mean Doppler velocity and spectrum width. The median velocity profile for coupled clouds (Fig. 16a) increases from inversion base until close to the surface. In the cloud layer this behavior is expected as hydrometeor sizes increase through collisions and diffusional growth in the cloud interior, leading to the larger hydrometeors with greater fall speeds falling from the cloud. In the sub-cloud layer, further increases in mean Doppler velocity indicate a continued growth of precipitation particles until approaching the surface. For the weakly decoupled state (Fig. 16b) this increase that starts from inversion base, stops near the decoupling height and the Doppler velocity becomes constant below that level. For the strongly decoupled clouds (Fig. 16c) the Doppler velocity increases abruptly slightly below the cloud base and then becomes quasi-steady through the entire sub-cloud

ACPD
14, 3815–3874, 2014

layer, including above and below the decoupling height. The RFD maximum frequencies for these cases are distributed around 0 m s^{-1} in the upper part of the cloud layer, suggesting that the returns in this area are from the cloud liquid. Moving downward in the liquid layer the slowly increasing downward velocity is due to the fact that ice starts to become relatively more abundant and more important in the total backscatter. The quasi-constant Doppler velocity below the decoupling height is a similar feature for both decoupled states; the ceased acceleration of hydrometeors at the decoupling height could be connected with evaporation/sublimation occurring locally. The stable cloud states (Fig. 16d) exhibit a totally different vertical structure where Doppler velocity is distributed around zero throughout both cloud and sub-cloud layer. The median profile is also close to zero, suggesting that no mean vertical motions occur either in the cloud or in the sub-cloud layer; essentially this means that clouds in the stable state have negligible precipitation.

The Doppler spectrum width (Fig. 17) is generally increasing from inversion base down to cloud base for all cloud states, except for stable clouds (Fig. 17d), suggesting that with decreasing height, the variability in hydrometeor size also increases within the cloud layer. Below cloud base, spectrum width decreases downwards; this decrease is sharper for decoupled clouds and especially those that are strongly decoupled (Fig. 17c). The rather quick decrease in spectrum width below the cloud base in the latter cases is probably due to the fact that there is less ice precipitation in these clouds and/or the deeper SML allows for increased sublimation of the smallest ice crystals, leading to a narrower Doppler spectrum.

Again, stable clouds (Fig. 17d) exhibit a totally different behavior than the other cases. The larger spectrum width frequencies are distributed around 0.2 m s^{-1} with an increasing spread towards higher values with decreasing height. These substantially smaller values in the cloud layer, compared to the neutrally-stratified clouds, are an additional indication that stable clouds are often not mixed-phase, while the slightly higher spread combined with near zero average velocities reveals that the lower part of the sub-cloud layer is slightly more turbulent than the cloud layer.

ACPD
14, 3815–3874, 2014

Profiles of relative humidity (with respect to ice, RH_i), specific moisture (Q_v) and wind speed (U) (Figs. 18, 19 and 20) are analyzed from radiosoundings. Both Q_v and U exhibited a significant scatter in absolute values, reflecting changes in air mass, so a scaling method was applied: the scaled parameter (U'', Q_v'') is defined by subtracting the mean values in the layer between the surface and inversion base (or the cloud top for stable cases) from the actual values. RH_i is in a sense already a scaled variable by definition and does not require any normalization. The RFDs of the two scaled variables and RH_i are normalized with respect to height as previously.

The maximum frequency of RH_i is at or often above saturation in the cloud interior for all states (Fig. 18). This indicates that these clouds can support the coexistence of ice and liquid hydrometeors within the same volume, considering layer mean temperatures are often below freezing. In the coupled and stable states (Fig. 18a and d) RH_i decreases below cloud base until the surface where it is sub-saturated. This decrease is also observed in the decoupled cases (Fig. 18b and c) but only down to the decoupling height; below that level it either remains roughly constant (Fig. 18b) or increases again (Fig. 18c). The decrease in RH_i below the cloud base is the largest in the strongly decoupled cases (Fig. 18c) and a clear minimum is observed around the decoupling height, below 85 %. The general decreasing RH_i profile with decreasing height below cloud agrees with decreasing profiles of Doppler spectrum widths and reflectivities, indicating sublimation of falling ice crystals in the sub-cloud layer appears to be an ongoing process for the majority of the strongly decoupled cloud states.

Specific humidity (Fig. 19) is similar in all states, except stable cases (Fig. 19d), increasing with decreasing height from the inversion base until close to the surface. For decoupled states, the structure below the decoupling height is slightly different; specific humidity here is often quasi-constant, especially in the strongly decoupled state where this layer is substantially moister in water vapor than aloft; this moist environment could favor the formation of a lower cloud layer. Both coupled and decoupled cloud states (Fig. 19a–c) show that moisture increases above the temperature inversion near cloud top (e.g., Sedlar and Tjernström 2009; Sedlar et al., 2012), indicating a potential source

ACPD
14, 3815–3874, 2014

of moisture for these cloud layers. While all neutrally-stratified cases have the common feature of a general decrease in specific humidity with increasing height, the stable clouds (Fig. 19d) feature the exact opposite behavior; a general increase from near the surface to the cloud top. Only the layer close to the surface often appears slightly more moist; however, the sub-cloud layer is still less moist that the cloud layer and the air immediately above the cloud.

RFDs of wind speed profiles are given in Fig. 20. Wind speed is a highly variable component of the system; hence the RFDs appear more scattered. The median of coupled (Fig. 20a) and weakly decoupled clouds (Fig. 20b) are quite similar, with almost constant wind speed inside the cloud and an increase from the surface to the cloud base; for the coupled state, there is a very weak indication of a maximum at the cloud base, agreeing with vertical wind speed shear during coupled surface and cloud cases analyzed by Sedlar and Shupe (2013). In contrast, for the strongly decoupled state (Fig. 20c), the median increases below cloud base and reaches a maximum close to the decoupling height, and then decreases towards the surface. Although this structure consists of many uniquely varying profiles, it indicates the presence of low-level jets (LLJ) in some of them. Studies on the nocturnal low-level jet have shown that it plays an important role in shear production in the layer between the LLJ maximum and the surface, which is an important source of turbulence (Mahrt et al., 1979; Tjernström and Smedman, 1993). The existence of these LLJs might explain the slightly higher momentum fluxes observed earlier in the decoupled cases (Fig. 8). The fact that the LLJ core occurs close to the decoupling height, where an inversion usually exists (see Fig. 14c), has been also observed in previous studies of nocturnal LLJs (Andreas et al., 2000; Jakobson et al., 2013). Finally, for the stable cloud state (Fig. 20d), median wind speed is similar to the coupled state, only the wind speed starts to decrease already from the cloud interior. However, the bimodal structure of the RFD in the sub-cloud layer indicates the presence of that LLJ also here, with an occurrence of about half the time.

ACPD
14, 3815–3874, 2014

4 Discussion

Here we present a summary of the main findings from this study. Neutrally-stratified clouds are usually mixed-phase, precipitating clouds, more frequently decoupled from the surface than coupled to it. In general, decoupled clouds are higher than coupled; analysis revealed that clouds with tops below 700 m tend to get coupled to the surface, whereas those whose tops are above 900 m remain decoupled from it. No differences were observed in geometric thickness or condensed water properties between the two states. Moreover, the surface fluxes are similar for both states, suggesting that the observed cloud thermodynamic state is not driven by changes in the magnitude, or sign, of the surface fluxes, in support of similar results in Shupe et al. (2013). It is more likely that displacements downwards (upwards) of the cloud layer is the leading factor that results in coupling (decoupling), which would instead be related more to the mesoscale weather patterns and advected thermodynamics (e.g., Sedlar and Shupe, 2013).

For decoupled clouds, the depth of the cloud-driven mixed layer increases with increasing cloud base and top, thus higher clouds tend to have deeper sub-cloud mixed layers (SML). Decoupled clouds exhibit a differentiation in thermodynamic structure, depending on the depth of the SML; those with SML less than 450 m are disconnected from the surface with weak inversions, whereas the clouds with SML greater than 500 m are characterized by stronger inversions at the decoupling height. The "weakly decoupled" cases occur twice as often compared to the "strongly decoupled".

Apart from the thermodynamic differences between the coupled and the two decoupled sub-categories, some microphysical differences were also observed. For the strongly decoupled cases, the reflectivity profiles exhibit a decrease inside the cloud, close to the cloud base and a bimodality in reflectivity distribution in the sub-cloud layer. One branch of the distribution indicates a large reflectivity decrease with decreasing height. This indicates that these clouds sometimes have little ice so that liquid dominates the radar signal in the cloud interior, whereas in the sub-cloud layer precipita-

ACPD
14, 3815–3874, 2014

tion undergoes evaporation/sublimation. In contrast, for coupled and weakly decoupled cases the reflectivity remains almost constant throughout both cloud and sub-cloud layer.

In addition, in strongly decoupled cases the sub-cloud mixed layer is significantly drier; coupled and weakly decoupled RH_i profiles decrease by only a few percent in the sub-cloud layer, while in strongly decoupled profiles it reaches a minimum around 85 %. Moreover, RH_i reaches its minimum at the decoupling height and below that it increases again, suggesting that the vertical level at which the cloud gets disconnected from the surface could be impacted by evaporation/sublimation. This hypothesis is also supported by the fact that increasing mean Doppler velocity with decreasing height ceases at the decoupling height in both decoupled sub-categories, which suggests that the hydrometeors do not grow below that level; on the contrary, in coupled cases the hydrometeors continue growing through the whole sub-cloud layer. We speculate that evaporation/sublimation may play some role in the decoupling process, by absorbing latent heat and stabilizing the atmosphere at that level. For example, in the case of strongly decoupled clouds the decoupling might be amplified because of the existence of a substantially warmer and moister layer capped by the lower inversion, which releases upward latent heat flux, which probably helps in sustaining the mixed layer over a larger depth above the decoupling height, as drier, colder cloud-driven eddies come into contact with warmer and moisture air near the decoupling height. On the other hand, the fact that precipitation falls through a deeper layer might be the primary reason why evaporation/sublimation appears more effective in strongly decoupled cases, compared to the weakly decoupled. Nevertheless, evaporation/sublimation may enhance the decoupling state, but yet this depends on where it occurs and actually on how much of it occurs; we must note that for some of the strongly decoupled cases, radar reflectivties are relatively low within the sub-cloud layers, suggesting smaller concentrations of precipitation hydrometeors.

Stably-stratified clouds differ substantially from the neutrally-stratified clouds; they are geometrically the thinnest clouds observed and are also very low, usually with

ACPD
14, 3815–3874, 2014

bases $< \sim 200$ m. The observed water properties indicate that these clouds are optically thin, with few droplets; the LWP is often $< \sim 50\,\mathrm{g\,m^{-2}}$, suggesting that stable clouds don't contain enough liquid to drive efficient in-cloud mixing, whereas the IWP is close to zero, indicating that they are often not mixed-phase or with very few precipitating ice crystals. A median LWP of $32\,\mathrm{g\,m^{-2}}$ for stable cases should be more than sufficient for producing localized radiative cooling and promoting droplet condensation, especially near cloud top where specific humidity is shown to increase. The main unanswered question is the distribution of the liquid water in the vertical, e.g. the liquid water content profile. Considering the lack of in-cloud mixing to destabilize the thermodynamic profile, the liquid may not be concentrated in a thin layer but rather be distributed more homogenously across the cloud, as hypothesized by Sedlar et al. (2012) for the portion of cloud layers that extend within a stable temperature inversion. Furthermore, the CCN concentrations are small in these cases, further supporting that stable clouds are optically thin; this assumes that the CCN concentrations nearer the surface are representative of in-cloud distributions, an assumption that may not hold neither when the entire surface-cloud layer is stably stratified nor when the clouds are decoupled. de Boer et al. (2011) suggests that liquid droplets may be an important driver for ice nucleation at temperatures above $-25\,^{\circ}\mathrm{C}$; the fact that such small liquid amounts are accompanied by very few or no ice particles in these clouds is consistent with the above theory.

The potential temperature gradient profiles in these stable cases show that surface turbulence usually does not impact the stable clouds and the specific humidity profiles, with increasing moisture with increasing height, indicate that the surface does not serve as a moisture source for them. The observed Doppler velocities are close to zero suggesting that these clouds are often non-precipitating. The magnitudes of the Doppler spectrum width are very small, which also supports the conclusion that stable clouds are usually not mixed-phase and have little turbulence. The evolution of these clouds could potentially follow two paths: (1) they increase in optical thickness through more liquid condensate, and potentially more CCN to activate upon, sufficient to drive

ACPD
14, 3815–3874, 2014

turbulent motions; these motions may connect with surface-generated turbulence, considering that the stable clouds are often in very close proximity to the surface (~ below 200 m) – thus eventually transitioning to a coupled cloud state. (2) They become more and more tenuous until they dissipate. In the first case, increased moisture and aerosol particles would be necessary.

5 Conclusions

Arctic low-level clouds and Arctic boundary layer structure have been examined, using observations from the ASCOS expedition, in late summer 2008. In particular, this study focuses on the interactions between low-level clouds and the surface; profiles of equivalent potential temperature are used to identify neutrally-stratified clouds that are thermodynamically "coupled" to, or "decoupled" from, the surface turbulence. Apart from these two cases, where turbulence is generated inside the cloud, a significant number of stably-stratified cases are also observed, suggesting the absence of in-cloud mixing for these cases. The vertical structure and properties of these three types: decoupled, coupled and stable clouds, is investigated. This study shows that:

- Decoupled clouds occur more frequently than coupled. The coupling state is primarily driven by the cloud, through turbulence generated in the cloud by radiative cooling and buoyant processes and is determined by the proximity of the cloud layer to the surface mixed layer. Surface fluxes seem to simply respond to the cloud processes aloft.
- Decoupled clouds exhibit a bimodality in their thermodynamic structure, associated with the depth of the sub-cloud mixed layer (SML); clouds with shallower SMLs are weakly decoupled from the surface, whereas higher clouds with relatively deeper SMLs are strongly decoupled. The enhancement of the decoupling is possibly due to evaporation/sublimation processes occurring within the SML.

ACPD
14, 3815–3874, 2014

– Stable clouds differ substantially from all neutrally-stratified states in both thermodynamic and microphysical structure, as well as in geometry and water properties. They are geometrically and optically thin clouds, often single-phase liquid with no or negligible precipitation falling out. Some of these cases, based on their proximity to the surface and tenuous nature, represent fog.

Further testing of these conclusions and potential links between the in-cloud dynamics and the cloud and precipitation microphysics, including feedbacks and forcing of the thermodynamic structure, should be further explored using modeling tools. Also, while this study illustrates the power of surface based remote sensing techniques, more direct in-situ profiling from the surface and through the clouds to determine the nature of the coupling would be highly advantageous.

Acknowledgements. The Arctic Summer Cloud-Ocean Study (ASCOS) was an IPY project under the AICI-IPY umbrella and an endorsed SOLAS project. ASCOS was made possible by funding from the Knut and Alice Wallenberg Foundation, the DAMOCLES Integrated Research Project, EU 6th Framework Program, while the Swedish Polar Research Secretariat (SPRS) provided access to the icebreaker *Oden* and logistical support. Support from the US National Science Foundation (NSF) and the National Atmospheric and Oceanic Administration (NOAA) for remote sensing instruments is gratefully acknowledged. MT & JS were funded by the Swedish National Research Council, the Bert Bolin Center for Climate Research and DAMOCLES. IMB was funded by the UK Natural Environment Research Council while MDS and POGP were funded by the NSF. GS was supported by the Office of Naval Research. Finally we are greatly indebted to the *Oden's* Captain Mattias Peterson and his crew for invaluable assistance with many things during ASCOS.

References

ACIA: Impacts of a warming Arctic: Arctic Climate Impact Assessment, Cambridge University Press, 2005.

Andreas, E. L., Claffey, K. J., and Makshtas, A. P.: Low-level atmospheric jets and inversions over the western Weddell Sea, Bound.-Lay. Meteorol., 97, 459–486, 2000.

ACPD
14, 3815–3874, 2014

Andreas, E. L., Jordan, R. E., and Makshtas, A. P.: Parameterizing turbulent exchange over sea ice: the ice station weddell results, Bound.-Lay. Meteorol., 114, 439–460, 2005.
Bigg, E. K. and Leck, C.: Cloud-active particles over the central Arctic Ocean, J. Geophys. Res., 106, 32155–32166, 2001.
Bony, S. and Dufresne, J. L.: Marine boundary layer clouds at the heart of tropical cloud feedback uncertainties in climate models, Geophys. Res. Lett., 32, L20806, doi:10.1029/2005GL023851, 2005.
Comiso, J. C.: A rapidly declining Arctic Perennial Ice Cover, Geophys Res. Lett., 29, 1956, doi:10.1029/2002GL015650, 2002.
Curry, J. A.: Interactions among turbulence, radiation and micro-physics in Arctic stratus clouds, J. Atmos. Sci., 43, 90–106, 1986.
Curry, J. A. and Ebert, E. E.: Annual cycle of radiative fluxes over the Arctic Ocean: sensitivity to cloud optical properties, J. Climate, 5, 1267–1280, 1992.
Curry, J. A., Rossow, W. B., Randall, D., and Schramm, J. L.: Overview of Arctic cloud and radiation characteristics, J. Climate, 9, 1731–1764, 1996.
de Boer, G., Morrison, H., Shupe, M. D., and Hildner, R.: Evidence of liquid dependent ice nucleation in high-latitude stratiform clouds from surface remote sensors, Geophys. Res. Lett., 38, L01803, doi:10.1029/2010GL046016, 2011.
Devasthale, A., Sedlar, J., Koenigk, T., and Fetzer, E. J.: The thermodynamic state of the Arctic atmosphere observed by AIRS: comparisons during the record minimum sea ice extents of 2007 and 2012, Atmos. Chem. Phys., 13, 7441–7450, doi:10.5194/acp-13-7441-2013, 2013.
Frisch, A. S., Fairall, C. W., and Snider, J. B.: Measurement of stratus cloud and drizzle parameters in ASTEX with a Kα-band doppler radar and a microwave radiometer, J. Atmos. Sci., 52, 2788–2799, 1995.
Graversen, R. G., Mauritsen, T., Tjernström, M., Källen, E., and Svensson, G.: Vertical structure of recent Arctic warming, Nature 451, 53–57, 2008.
Intrieri, J. M., Shupe, M. D., Uttal, T., and McCarty, B. J.: An annual cycle of Arctic clouds characteristics observed by radar and lidar at SHEBA, J. Geophys. Res., 107, 8030, doi:10.1029/2000JC000423, 2002.
Jakobson, L., Vihma, T., Jakobson, E., Palo, T., Männik, A., and Jaagus, J.: Low-level jet characteristics over the Arctic Ocean in spring and summer, Atmos. Chem. Phys., 13, 11089–11099, doi:10.5194/acp-13-11089-2013, 2013.

ACPD
14, 3815–3874, 2014

Kahl, J. D., Serreze, M. C., and Schnell, R. C.: Low-level tropospheric temperature inversions in the Canadian Arctic, Atmos. Ocean, 30, 511–529, 1992.
Karlsson, J. and Svensson, G.: The simulation of Arctic clouds and their influence on the winter surface temperature in present-day climate in the CMIP3 multi-model dataset, Clim. Dynam., 36, 623–635, doi:10.1007/s00382-010-0758-6, 2010.
Kapsch, M., Graversen, R. G., and Tjernström, M.: Springtime atmospheric energy transport and the control of Arctic summer sea-ice extent, Nature Clim. Change, 3, 744–748, doi:10.1038/nclimate1884, 2013.
Kay, J. E. and Gettelman, A.: Cloud influence on and response to seasonal Arctic sea ice loss, J. Geophys. Res., 114, D18204, doi:10.1029/2009JD011773, 2009.
Korolev, A.: Limitations of the Wegener–Bergeron–Findeisen mechanism in the evolution of mixed-phase clouds, J. Atmos. Sci., 64, 3372–3375, 2007.
Lauer, A., Hamilton, K., Wang, Y., Phillips, V. T. J., and Bennartz, R.: The impact of global warming on marine boundary layer clouds over the Eastern Pacific – a regional model study, J. Climate, 23, 5844–5863, 2010.
Leck, C., Norman, M., Bigg, E. K., and Hillamo, R.: Chemical composition and sources of the high Arctic aerosol relevant for fog and cloud formation, J. Geophys. Res., 107, 4135, doi:10.1029/2001JD001463, 2002.
Leck, C., Tjernström, M., Matrai, P., Swietlicki, E., and Bigg, K.: Can marine micro-organisms influence melting of the Arctic pack ice? EOS, 85, 25–36, 2004.
Lindsay, R. W., Zhang, J., Schweiger, A. J., Steele, M. A., and Stern, H.: Arctic sea ice retreat in 2007 follows thinning trend, J. Climate, 22, 165–176, doi:10.1175/2008JCLI2521.1,, 2009.
Mahrt, L., Heald, R. C., Lenschow, D. H., Stankov, B. B., and Troen, I.: An observational study of the structure of the nocturnal boundary layer, Bound.-Lay. Meteorol., 17, 247–264, 1979.
Martin, M., Chang, R. Y.-W., Sierau, B., Sjogren, S., Swietlicki, E., Abbatt, J. P. D., Leck, C., and Lohmann, U.: Cloud condensation nuclei closure study on summer arctic aerosol, Atmos. Chem. Phys., 11, 11335–11350, doi:10.5194/acp-11-11335-2011, 2011.
Maslanik, J. A., Fowler, C., Stroeve, J., Drobot, S., Zwally, J., Yi, D., and Emery, W.: A younger, thinner Arctic ice cover: Increased potential for rapid, extensive sea-ice loss, Geophys. Res. Lett., 34, L24501, doi:10.1029/2007GL032043, 2007.
Mauritsen, T., Sedlar, J., Tjernström, M., Leck, C., Martin, M., Shupe, M., Sjogren, S., Sierau, B., Persson, P. O. G., Brooks, I. M., and Swietlicki, E.: An Arctic CCN-limited cloud-aerosol regime, Atmos. Chem. Phys., 11, 165–173, doi:10.5194/acp-11-165-2011, 2011.

ACPD
14, 3815–3874, 2014

Moran, K. P., Martner, B. E., Post, M. J., Kropfli, R. A., Welsh, D. C., and Widener, K. B.: An unattended cloud-profiling radar for use in climate research. B. Am. Meteorol. Soc., 79, 443–455, 1998.

Morrison, H., de Boer, G., Feingold, G., Harrington, J., Shupe, M. D., and Sulia, K.: Resilience of persistent Arctic mixed-phase clouds, Nat. Geosci., 5, 11–17, doi:10.1038/NGEO1332, 2012.

Nghiem, S. V., Rigor, I. G., Perovich, D. K., Clemente-Colon, P., Weatherly, J. W., and Neumann, G.: Rapid reduction of Arctic perennial sea ice, Geophys. Res. Lett., 34, L19504, doi:10.1029/2007GL031138, 2007.

Nicholls, S.: The dynamics of stratocumulus: Aircraft observations and comparisons with a mixed layer model, Q. J. Roy. Meteor. Soc., 110, 783–820, doi:10.1002/qj.49711046603, 1984.

Overland, J. E., Spillane, M. C., Percival, D. B., Wang, M., and Mofjeld, H. O.: Seasonal and regional variation of pan-Arctic surface air temperature over the instrumental record, J. Climate, 15, 3263–3282, 2004.

Perovich, D. K., Richter-Menge, J. A., Jones, K. F., and Light, B.: Sunlight, water, and ice: extreme Arctic sea ice melt during the summer of 2007, Geophys. Res, Lett., 35, L11501, doi:10.1029/2008GL034007, 2008.

Persson, P. O. G., Fairall, C. W., Andreas, E. L., Guest, P. S., and Perovich, D. K.: Measurements near the Atmospheric Surface Flux Group tower at SHEBA: near-surface conditions and surface energy budget, J. Geophys. Res., 107, 1–21, doi:10.1029/2000JC000705, 2002.

Pinto, J. O.: Autumnal mixed-phase cloudy boundary layers in the Arctic, J. Atmos. Sci., 55, 2016–2038, 1998.

Pinto, J. O. and Curry, J. A.: Atmospheric convective plumes emanating from leads: 2. Microphysical and radiative processes, J. Geophys. Res., 100, 4633–4642, 1995.

Prenni, A. J., DeMott, P. J., Kreidenweis, S. M, Harrington, J. Y., Avramov, A., Verlinde, J., Tjernström, M., Long, C. N., and Olsson, P. Q.: Can Ice-Nucleating Aerosols Affect Arctic Seasonal Climate? B. Am. Meteorol. Soc., 88, 541–550, 2007.

Randall, D., Curry, J., Battisti, D., Flato, G., Grumbine, R., Hakkinen, S., Martinson, D., Preller, R., Walsh, J., and Weatherly, J.: Status of and outlook for large-scale modeling of atmosphere-ice-ocean interaction in the Arctic, B. Am. Meteorol. Soc., 79, 197–219, 1998.

Roberts, G. C. and Nenes, A. A: continuous-flow streamwise thermal-gradient CCN chamber for atmospheric measurements, Aerosol Sci. Tech., 39, 206–221, 2005.

ACPD
14, 3815–3874, 2014

Richter-Menge, J.: The Arctic, in: State of the Climate in 2009, B. Am. Meteorol. Soc., 91, 107–124, 2010.
Sedlar, J. and Shupe, M. D.: Characteristic nature of vertical motions observed in Arctic mixed-phase stratocumulus, Atmos. Chem. Phys. Discuss., 13, 31079–31125, doi:10.5194/acpd-13-31079-2013, 2013.
Sedlar, J. and Tjernström, M.: Stratiform Cloud-inversion characterization during the Arctic melt season, Bound.-Lay. Meteorol., 132, 455–474, doi:10.1007/s10546-009-9407-1, 2009.
Sedlar, J., Tjernström, M., Mauritsen, T., Shupe, M. D., Brooks, I. M., Persson, P. O. G., Birch, C. E., Leck, C., Sirevaag, A., and Nicolaus, M.: A transitioning Arctic surface energy budget: the impacts of solar zenith angle, surface albedo and cloud radiative forcing, Clim. Dynam., 37, 1643–1660, doi:10.1007/s00382-010-0937-5, 2011.
Sedlar, J., Shupe, M. D., and Tjernström, M.: On the relationship between thermodynamic structure, cloud top, and climate significance in the Arctic, J. Climate, 25, 2374–2393, 2012.
Serreze, M. C. and Barry, R. G.: Processes and impacts of Arctic amplification: a research synthesis, Global Planet. Change, 77, 85–96, doi:10.1016/j.gloplacha.2011.03.004, 2011.
Serreze, M. C. and Francis, J. A.: The arctic amplification debate, Climatic Change, 76, 241–264, doi:10.1007/s10584-005-9017-y, 2006.
Serreze, M. C., Walsh, J. E., Chapin III, F. S., Osterkamp, T., Dyurgerov, M., Romanovsky, V., Oechel, W. C., Morison, J., Zhang, T., and Barry, R. G.: Observational evidence of recent change in the northern high-latitude environment, Climatic Change, 46, 159–207, 2000.
Serreze, M. C., Holland, M. M., and Stroeve, J.: Perspectives on the Arctic's shrinking sea-ice cover, Science, 315, 1533–1536, doi:10.1126/science.1139426, 2007.
Shupe, M. D.: Clouds at Arctic atmospheric observatories, Part II: Thermodynamic phase characteristics, J. Appl. Meteorol. Clim., 50, 645–661, 2011.
Shupe, M. D. and Intrieri, J. M.: Cloud radiative forcing of the Arctic surface: the influence of cloud properties, surface albedo, and solar zenith angle, J. Climate, 17, 616–628, 2004.
Shupe, M. D., Uttal, T., and Matrosov, S. Y.: Arctic cloud microphysics retrievals from surface-based remote sensors at SHEBA, J. Appl. Meteorol. Clim., 44, 1544–1562, 2005.
Shupe, M. D., Kollias, P., Persson, P. O. G., and McFarquhar, G. M.: Vertical motions in Arctic mixed-phase stratiform clouds, J. Atmos. Sci., 65, 1304–1322, 2008.
Shupe, M. D., Walden, V. P., Eloranta, E., Uttal, T., Campbell, J. R., Starkweather, S. M., and Shiobara, M.: Clouds at Arctic atmospheric observatories, Part I: Occurrence and macrophysical properties, J. Appl. Meteorol. Clim., 50, 626–644, 2011.

ACPD
14, 3815–3874, 2014

Shupe, M. D., Persson, P. O. G., Brooks, I. M., Tjernström, M., Sedlar, J., Mauritsen, T., Sjogren, S., and Leck, C.: Cloud and boundary layer interactions over the Arctic sea ice in late summer, Atmos. Chem. Phys., 13, 9379–9399, doi:10.5194/acp-13-9379-2013, 2013.
Simmonds, I. and Rudeva, I.: The great Arctic cyclone of August 2012, Geophys. Res. Lett., 39, L23709, doi:10.1029/2012GL054259, 2012.
Stephens, G. L.: Radiation profiles in extended water clouds. I. I. Parameterization schemes. J. Atmos. Sci., 35, 2123–2132, 1978.
Stroeve, J., Holland, M., Meier, W., Scambos, T., and Serreze, M.: Arctic sea ice decline: faster than forecast, Geophys. Res. Lett., 34, L09501, doi:10.1029/2007GL029703, 2007.
Stroeve, J. C., Serreze, M. C., Holland, M. M., Kay, J. E., Maslanik, J., and Barrett, A. P.: The Arctic's rapidly shrinking sea ice cover: a research synthesis, Clim. Change, 110, 1005–1027, 2012.
Tjernström, M.: The summer Arctic boundary layer during the Arctic Ocean Experiment 2001 (AOE-2001). Bound. Layer Meteorol., 117, 5–36, 2005.
Tjernström, M. and Smedman, A.-S.: The vertical turbulence structure of the coastal marine atmospheric boundary layer. J. Geophys. Res., 98, 4809–4826, 1993.
Tjernström, M., Leck, C., Persson, P. O. G., Jensen, M. L., Oncley, S. P., and Targino, A.: The summertime Arctic atmosphere: Meteorological measurements during the Arctic Ocean Experiment (AOE-2001). B. Am. Meteorol. Soc., 85, 1305–1321, 2004a.
Tjernström, M., Leck, C., Persson, P. O. G., Jensen, M. L., Oncley, S. P., and Targino, A.: Experimental equipment: an electronic supplement to "The summertime Arctic atmosphere: Meteorological measurements during the Arctic Ocean Experiment (AOE-2001)". B. Am. Meteorol. Soc., 85, 1322–1322, 2004b.
Tjernström, M., Zagar, M., Svensson, G., Cassano, J. C., Pfeifer, S., Rinke, A, Wyser, K., Dethloff, K., Jones, C. Semmler, T., and Shaw, M.: Modelling the Arctic boundary layer: An evaluation of six ARCMIP regional-scale models using data from the SHEBA project. Bound. Layer Meteorol., 117, 337–381, 2005.
Tjernström, M., Sedlar, J., and Shupe, M. D.: How well do regional climate models reproduce radiation and clouds in the Arctic?, J. App. Meteorol. Clim., 47, 2405–2422, 2008.
Tjernström, M., Birch, C. E., Brooks, I. M., Shupe, M. D., Persson, P. O. G., Sedlar, J., Mauritsen, T., Leck, C., Paatero, J., Szczodrak, M., and Wheeler, C. R.: Meteorological conditions in the central Arctic summer during the Arctic Summer Cloud Ocean Study (ASCOS), Atmos. Chem. Phys., 12, 6863–6889, doi:10.5194/acp-12-6863-2012, 2012.

ACPD
14, 3815–3874, 2014

Tjernström, M., Leck, C., Birch, C. E., Brooks, B. J., Brooks, I. M., Bäcklin, L., Chang, R. Y.-W., Granath, E., Graus, M., Hansel, A., Heintzenberg, J., Held, A., Hind, A., de la Rosa, S., Johnston, P., Knulst, J., de Leeuw, G., Di Liberto, L., Martin, M., Matrai, P. A., Mauritsen, T., Müller, M., Norris, S. J., Orellana, M. V., Orsini, D. A., Paatero, J., Persson, P. O. G., Gao, Q., Rauschenberg, C., Ristovski, Z., Sedlar, J., Shupe, M. D., Sierau, B., Sirevaag, A., Sjogren, S., Stetzer, O., Swietlicki, E., Szczodrak, M., Vaattovaara, P., Wahlberg, N., Westberg, M., and Wheeler, C. R.: The Arctic Summer Cloud-Ocean Study (ASCOS): overview and experimental design, Atmos. Chem. Phys. Discuss., 13, 13541–13652, doi:10.5194/acpd-13-13541-2013, 2013.

Twomey, S. A.: The influence of pollution on the shortwave albedo of clouds, J. Atmos. Sci., 34, 1149–1152, 1977.

Uttal, T., Curry, J. A., Mcphee, M. G., Perovich, D. K., Moritz, R. E., Maslanik, J. A., Guest, P. S., Stern, H. L., Moore, J. A., Turenne, R., Heiberg, A., Serreze, M. C., Wylie, D. P., Persson, P. O. G., Paulson, C.A, Halle, C., Morison, J. H., Wheeler, P. A., Makshtas, A., Welch, H., Shupe, M. D., Intrieri, J. M., Stamnes, K., Lindsey, R. W., Pinkel, R., Pegau, W. S., Stanton, T. P., and Grenfeld, T. C.: Surface heat budget of the Arctic Ocean, B. Am. Meteorol. Soc., 83, 22 255–276, 2002.

Wang, X. and Key, J. R.: Arctic surface, cloud, and radiation properties based on the AVHRR polar pathfinder data set. Part I: Spatial and temporal characteristics, J. Climate, 18, 30 2558–2574, 2005.

Webb, M. J., Senior, C. A., Sexton, D. M. H., Ingram, W. J., Williams, K. D., Ringer, M. A., McAvaney, B. J., Colman, R., Soden„ B. J., Gudgel, R., Knutson, T., Emori, S., Ogura, T., Tsushima, Y., Andronova, N., Li, B., Musat, I., Bony, S., and Taylor, K. E.: On the contribution of local feedback mechanisms to the range of climate sensitivity in two GCM ensembles, Clim. Dynam., 27 17–38, doi:10.1007/s00382-006-0111-2, 2006.

Westwater, E. R., Han, Y., Irisov, V. G., Leuskiy, V., Kadygrov, E. N., and Viazankin, S. A.: Remote sensing of boundary layer temperature profiles by a scanning 5-mm microwave radiometer and RASS: Comparison experiments, J. Atmos. Ocean. Tech., 16, 805–818, 1999.

Westwater, E. R., Han, Y., Shupe, M. D., and Matrosov, S. Y.: Analysis of integrated cloud liquid and precipitable water vapor retrievals from microwave radiometers during SHEBA, J. Geophys. Res., 106, 32019–32030, 2001.

ACPD
14, 3815–3874, 2014

Zhang, J., Lindsay, R., Schweiger, A., and Steele, M.: The impact of an intense summer cyclone on 2012 Arctic sea ice retreat, Geophys. Res. Lett., 40, 720–726, doi:10.1002/grl.50190, 2013.

ACPD
14, 3815–3874, 2014

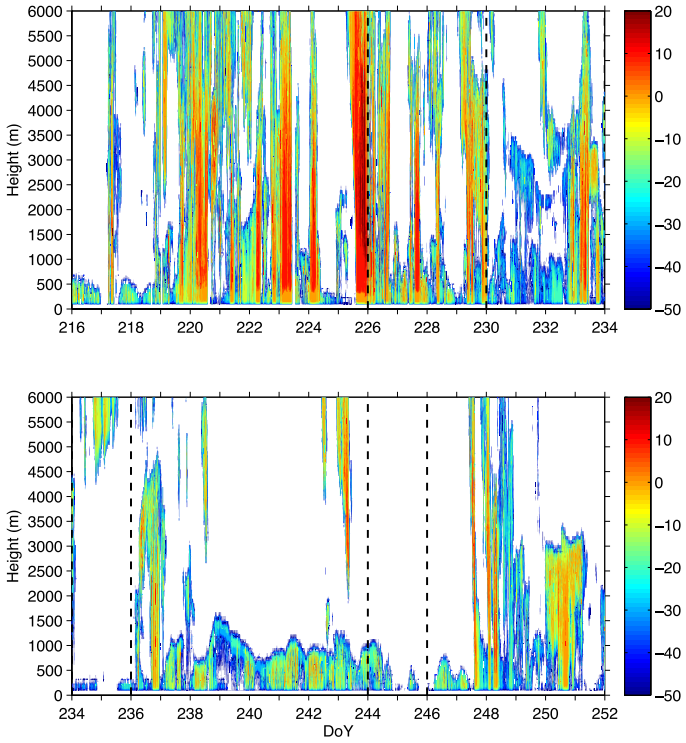

Fig. 1. Radar reflectivity contour [colors, dBZ] time-series for the ASCOS experiment, given in Day of Year (DoY) 2008. The vertical dashed lines differentiate the five periods of the ice drift (see Sect. 2.3 for a discussion on period characteristics). Periods prior to DoY 226 and after DoY 246 are the transit periods (before/after the ice drift). Reflectivity profiles are shown up to 6 km.

ACPD
14, 3815–3874, 2014

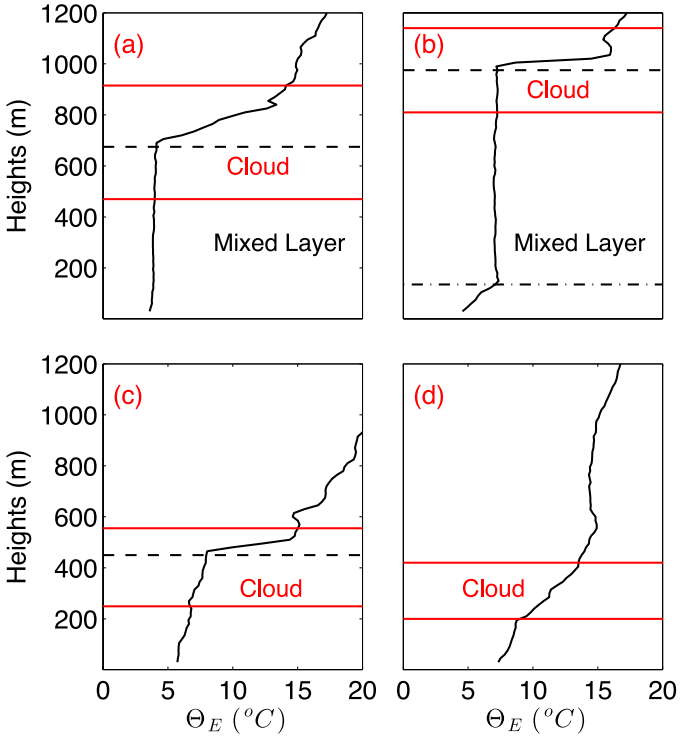

Fig. 2. Example profiles of scanning radiometer equivalent potential temperature (Θ_E) [°C] vertical profiles from four ASCOS cases: **(a)** coupled cloud [DoY 240, 20.16.47 p.m.], **(b)** decoupled cloud [DoY 239, 16.51.47 p.m.], **(c)** stable cloud (with inversion identified around cloud top) [DoY 217, 16.45.00 p.m.], **(d)** stable cloud (no inversion around cloud top) [DoY 251, 02.43.13 a.m.]. Red lines indicate the respective cloud boundaries observed at profile time. The inversion base height is shown as the black dashed line. The black dashed-dotted line indicates the decoupling height. The layer between dashed and dashed-dotted is defined as the mixed layer.

ACPD
14, 3815–3874, 2014

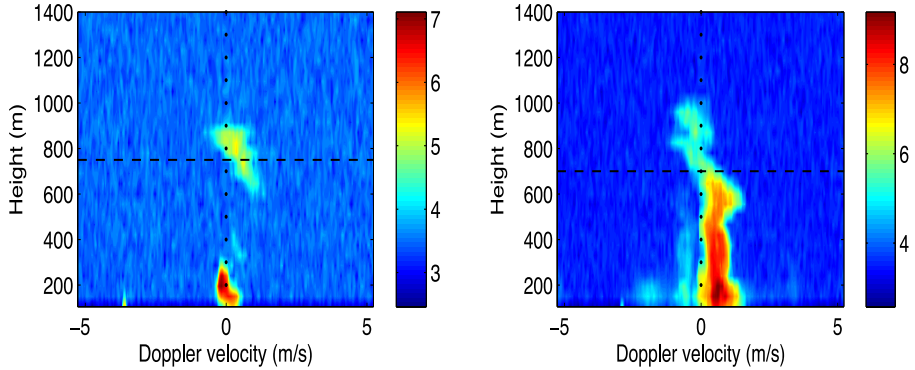

Fig. 3. Spectrographs for two ASCOS snapshots: **(a)** DoY 241, 19.11.52 p.m.: the cloud top median height observed by the MMCR is 960 m and the median cloud base height observed by the ceilometer is 90 m. We estimate the upper cloud base at 750 m from the spectrograph. **(b)** DoY 237, 10.11.40 a.m.: the cloud top median height is 1095 m and ceilometer median cloud base height is 140 m. We estimate the real base at 700 m. The horizontal black dashed lines indicate the qualitatively derived cloud base heights. Colors show the relative frequency distribution (logarithm of reflectivity counts) of spectral density of Doppler velocity with height. Positive (negative) values represent downward (upward) motion. Zero values are highlighted with dots.

ACPD
14, 3815–3874, 2014

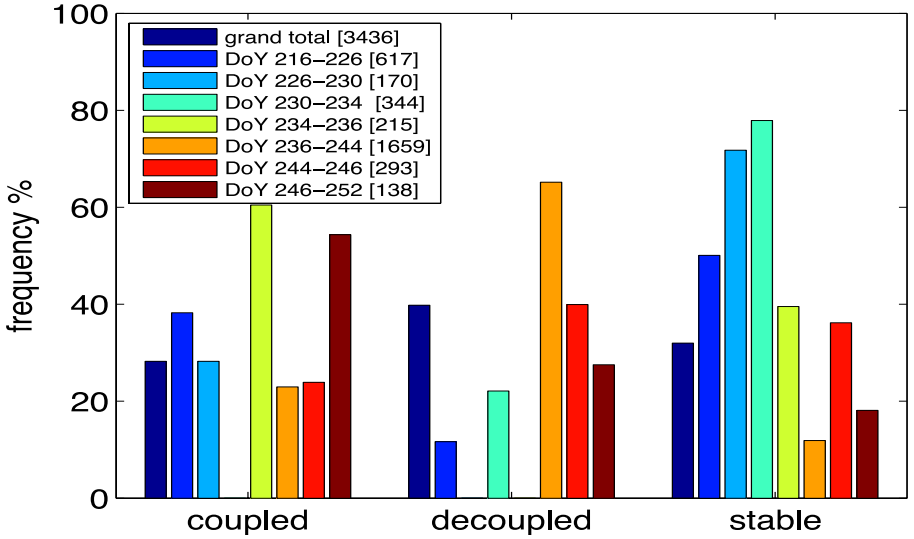

Fig. 4. Relative frequency distribution (RFD) of cloud state occurrence for each period of ASCOS. The number in the brackets indicates the total number of scanning radiometer profiles analysed for each period of ASCOS (see Sect. 2.3 for a discussion on period characteristics).

ACPD
14, 3815–3874, 2014

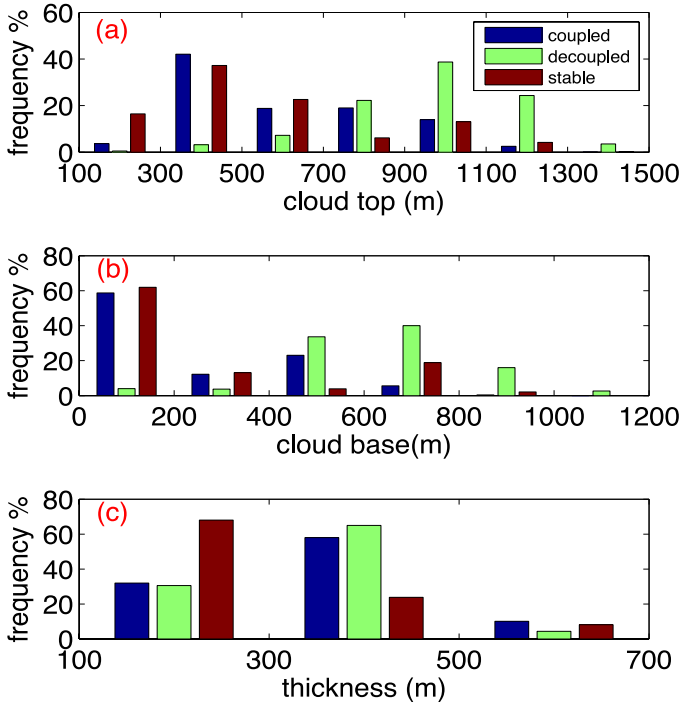

Fig. 5. RFDs of **(a)** cloud top height [m], **(b)** cloud base height [m] and **(c)** cloud thickness [m] for coupled (blue), decoupled (green) and stable (red) cloud states. Bin size is 200 m and centered in the interval.

ACPD
14, 3815–3874, 2014

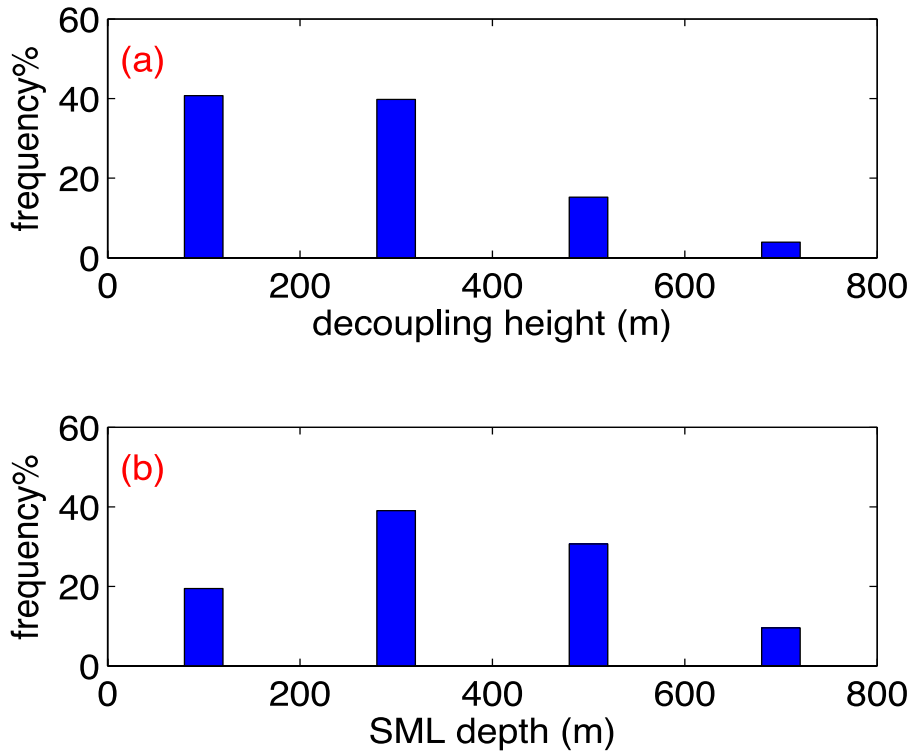

Fig. 6. RFDs of **(a)** the decoupling height [m] above the surface and **(b)** the sub-cloud mixed layer (SML) depth [m], defined as the difference between cloud base and decoupling height. Bin size is 200 m and centered in the interval.

ACPD
14, 3815–3874, 2014

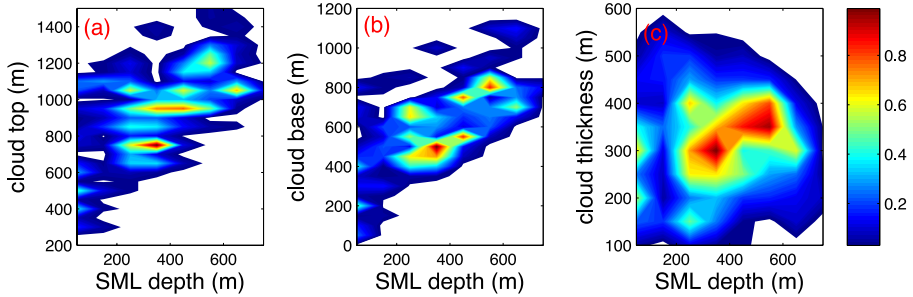

Fig. 7. 2-D RFD contour plots of **(a)** cloud top height [m], **(b)** cloud base height [m] and **(c)** cloud thickness [m] in relationship to sub-cloud mixed layer (SML) depth [m]. Frequencies are normalized to unity.

ACPD
14, 3815–3874, 2014

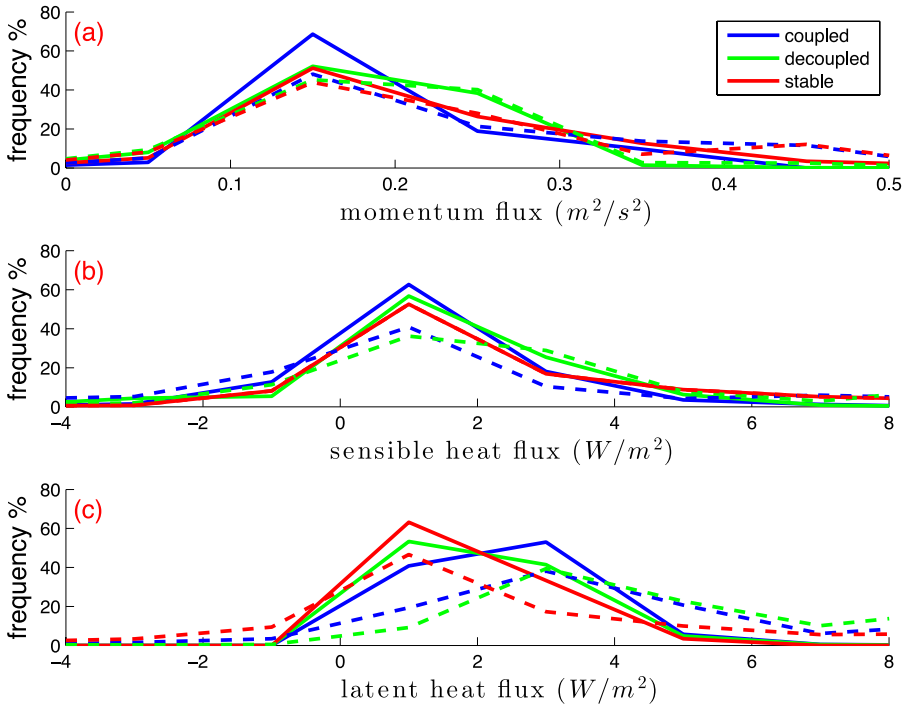

Fig. 8. RFDs of **(a)** momentum flux [$m^2\,s^{-2}$], **(b)** sensible heat flux [$W\,m^{-2}$] and **(c)** latent heat flux [$W\,m^{-2}$] for coupled (blue), decoupled (green) and stable (red) clouds. Solid lines represent fluxes estimated from sonic anemometers while dotted lines are the bulk fluxes; see Sect. 2.2 for a description on flux calculations.

ACPD
14, 3815–3874, 2014

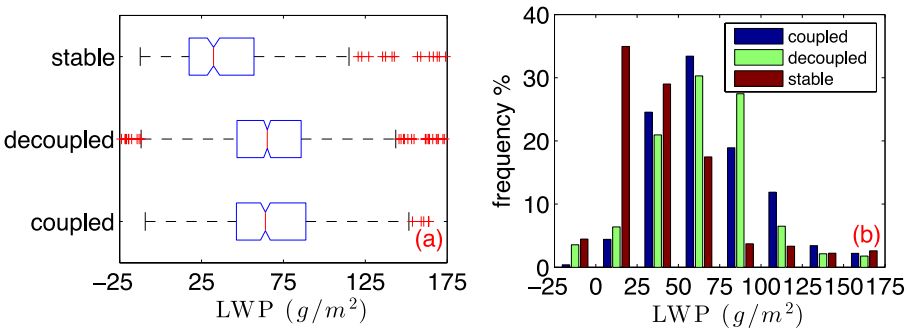

Fig. 9. (a) Notched box-and-whisker plots and **(b)** RFDs of LWP [g m^{-2}] for coupled, decoupled and stable single cloud layers. In **(a)**, median values are indicated by the red solid line, edges of the box mark the lower and upper quartiles, whiskers represent the extent of the data that is 1.5 times the difference between the upper and lower quartile and crosses are outliers. Notches offer a rough guide to significance of difference of medians; the width of the notches is proportional to the interquartile range of the sample and inversely proportional to the square root of the size of the sample. The bin size in **(b)** is 25 g m^{-2} and centered in the interval. Negative values are due to the instrument uncertainty of 25 g m^{-2}.

ACPD
14, 3815–3874, 2014

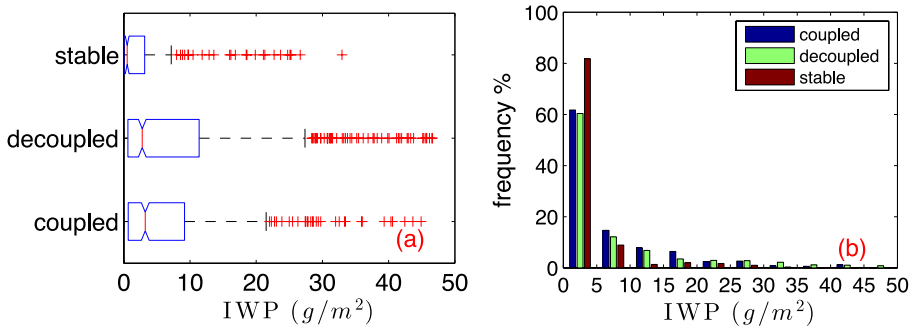

Fig. 10. Same as in Fig. 9, but for ice water path (IWP) [$g\,m^{-2}$] derived from radar power–law relationships. The bin size in **(b)** is $5\,g\,m^{-2}$ and centered in the interval.

ACPD
14, 3815–3874, 2014

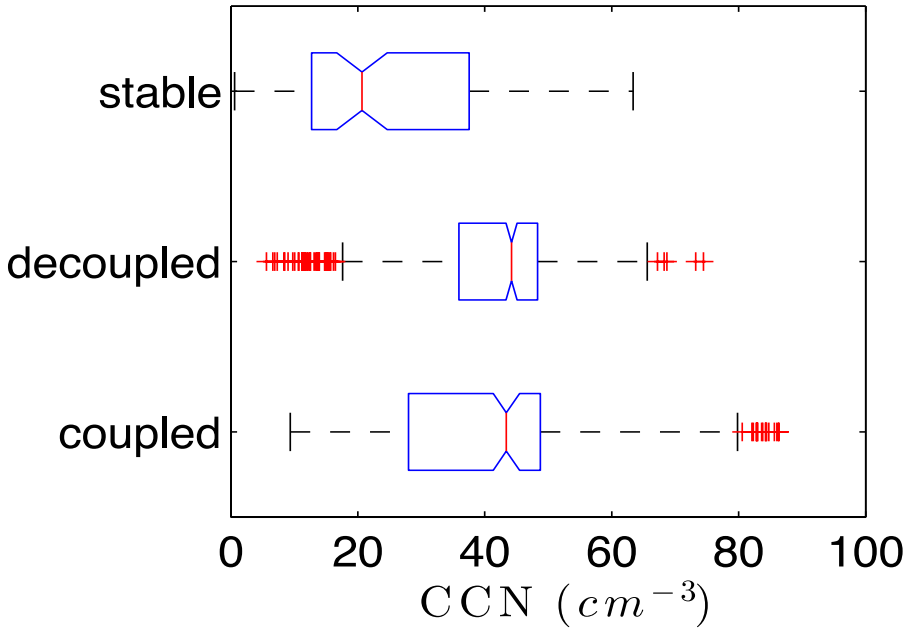

Fig. 11. Notched box-and-whisker plot of CCN concentrations [cm^{-3}] for coupled, decoupled and stable cloud layers. CCN concentrations are measured from ship level (see Martin et al., 2011).

ACPD
14, 3815–3874, 2014

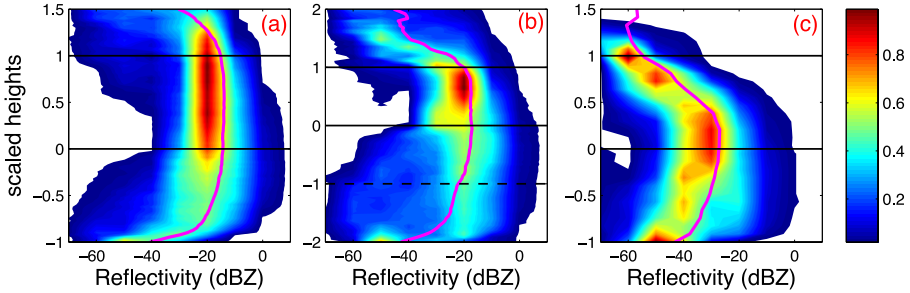

Fig. 12. RFD contour plots of radar reflectivity [dBZ] for **(a)** coupled, **(b)** decoupled and **(c)** stable clouds; magenta profiles are the medians. Heights are normalized: for **(a)** coupled clouds, $z_n = -1$ is the first range gate, $z_n = 0$ is cloud base and $z_n = 1$ is the main inversion base; for **(b)** decoupled clouds, $z_n = -2$ is the first range gate, $z_n = -1$ is the decoupling height, $z_n = 0$ is cloud base and $z_n = 1$ is main inversion base; for **(c)** stable clouds, $z_n = -1$ is the first range gate, $z_n = 0$ is cloud base and $z_n = 1$ is cloud top; reflectivity values above cloud top ($z_n = 1$) for **(c)** occur because stricter reflectivity thresholds were applied to identify cloud boundaries, while the full reflectivity profiles were used to compute the histogram statistics. Frequencies are normalized.

ACPD
14, 3815–3874, 2014

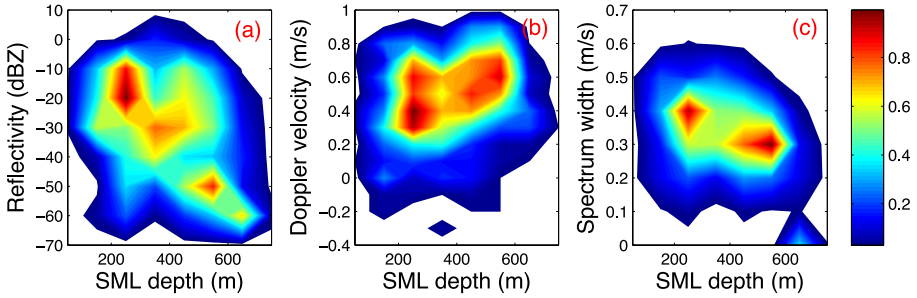

Fig. 13. 2-D RFD contour plots of **(a)** radar reflectivity [dBZ], **(b)** Doppler velocity [$m s^{-1}$] and **(c)** spectrum width [$m s^{-1}$] at the decoupling height, in relationship to the sub-cloud mixed layer (SML) depth [m]. Frequencies are normalized by unity.

ACPD
14, 3815–3874, 2014

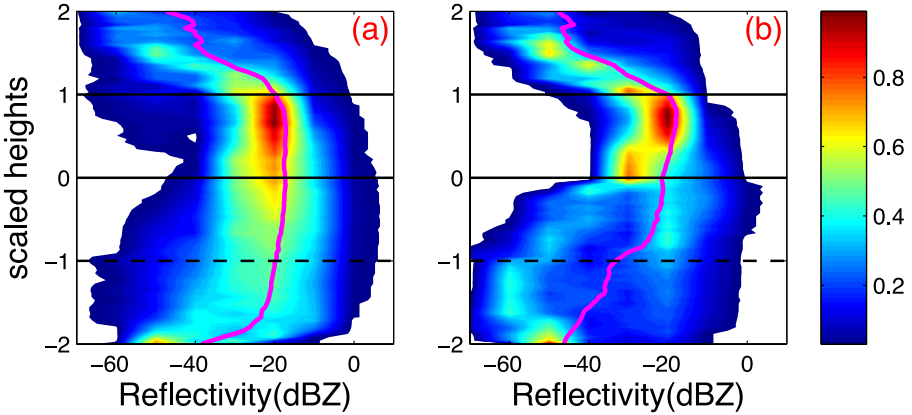

Fig. 14. Same as Fig. 12 but for **(a)** clouds decoupled less than 450 m below cloud base and **(b)** clouds decoupled more than 500 m below cloud base.

ACPD
14, 3815–3874, 2014

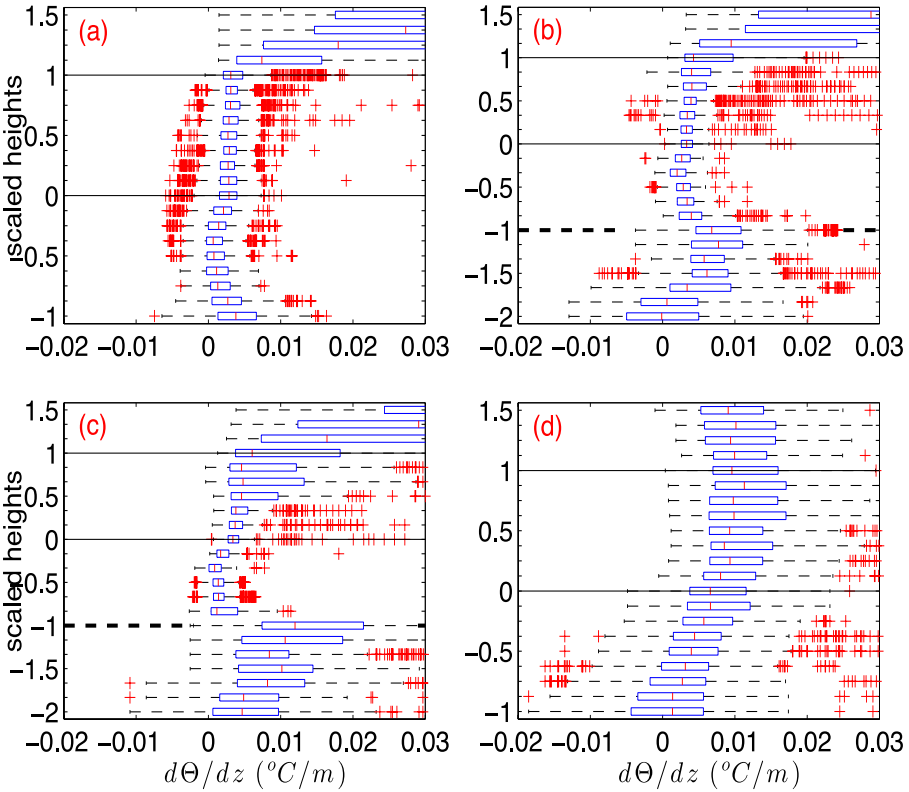

Fig. 15. Box-and-whisker plots of scanning radiometer potential temperature gradient $d\Theta dz^{-1}$ [°C m^{-1}] for **(a)** coupled, **(b)** weakly decoupled, **(c)** strongly decoupled and **(d)** stable clouds. The vertical scaling changes with cloud coupling state and is same as described in Fig. 12.

ACPD
14, 3815–3874, 2014

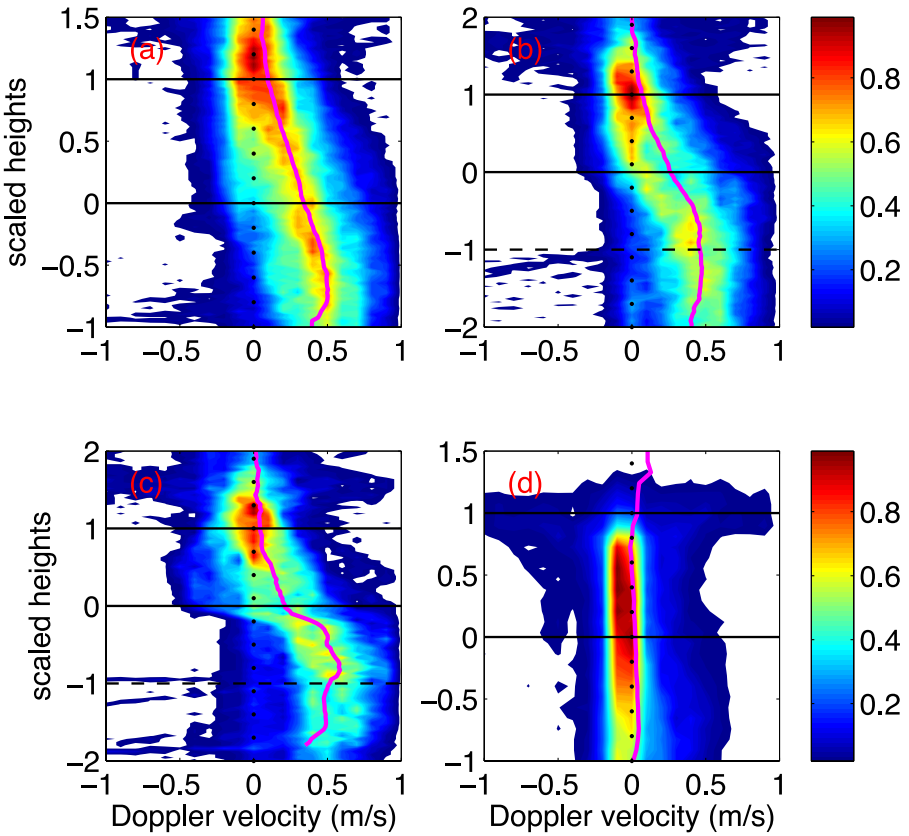

Fig. 16. RFD contour plots of Doppler velocity [m s^{-1}] for **(a)** coupled, **(b)** weakly decoupled, **(c)** strongly decoupled and **(d)** stable clouds; magenta profiles are the medians. The vertical scaling changes with cloud coupling state and is same as described in Fig. 12. Zero values are highlighted with dots.

ACPD
14, 3815–3874, 2014

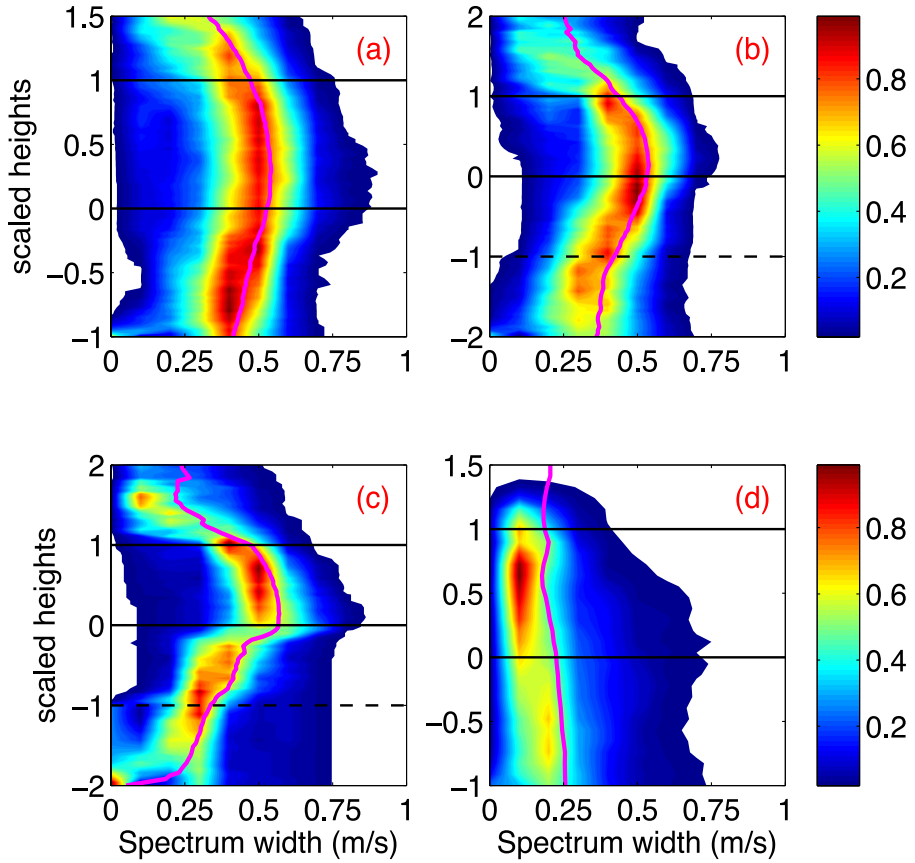

Fig. 17. Same as Fig. 16, but for spectrum width [$m s^{-1}$].

ACPD
14, 3815–3874, 2014

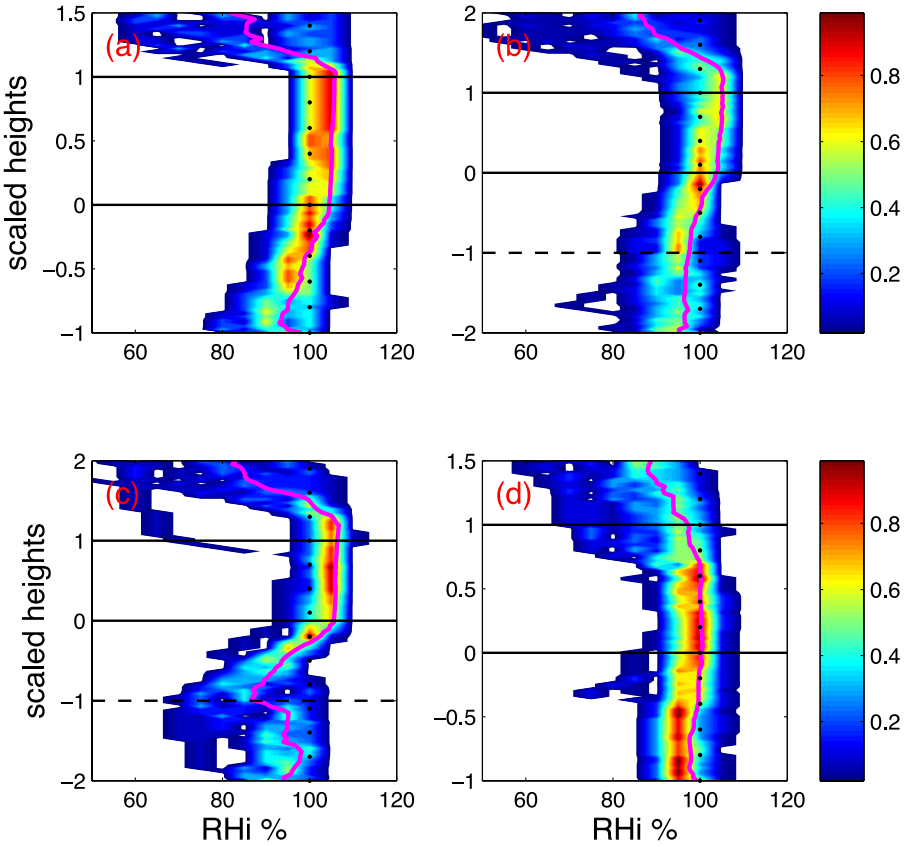

Fig. 18. Same as Fig. 16, but for radiosonde relative humidity [%] with respect to ice (RH_i). 100 % values are highlighted with dots.

ACPD
14, 3815–3874, 2014

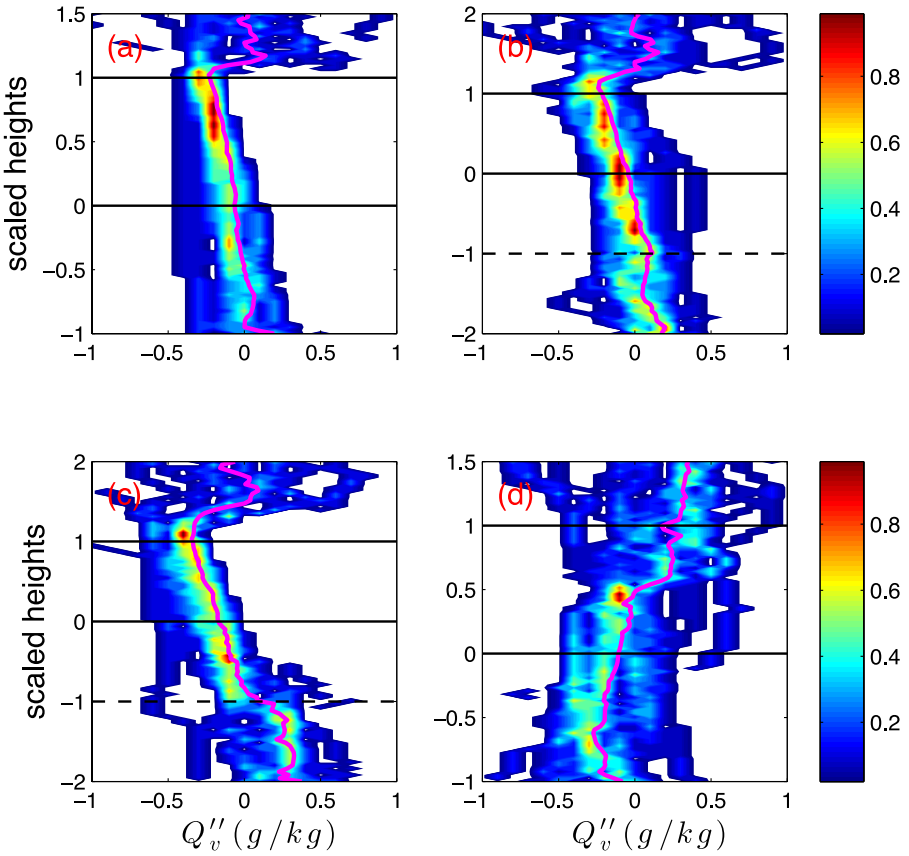

Fig. 19. Same as Fig. 16, but for radiosonde scaled specific humidity [g kg^{-1}]. See Sect. 3.5 for details on the scaling method.

ACPD
14, 3815–3874, 2014

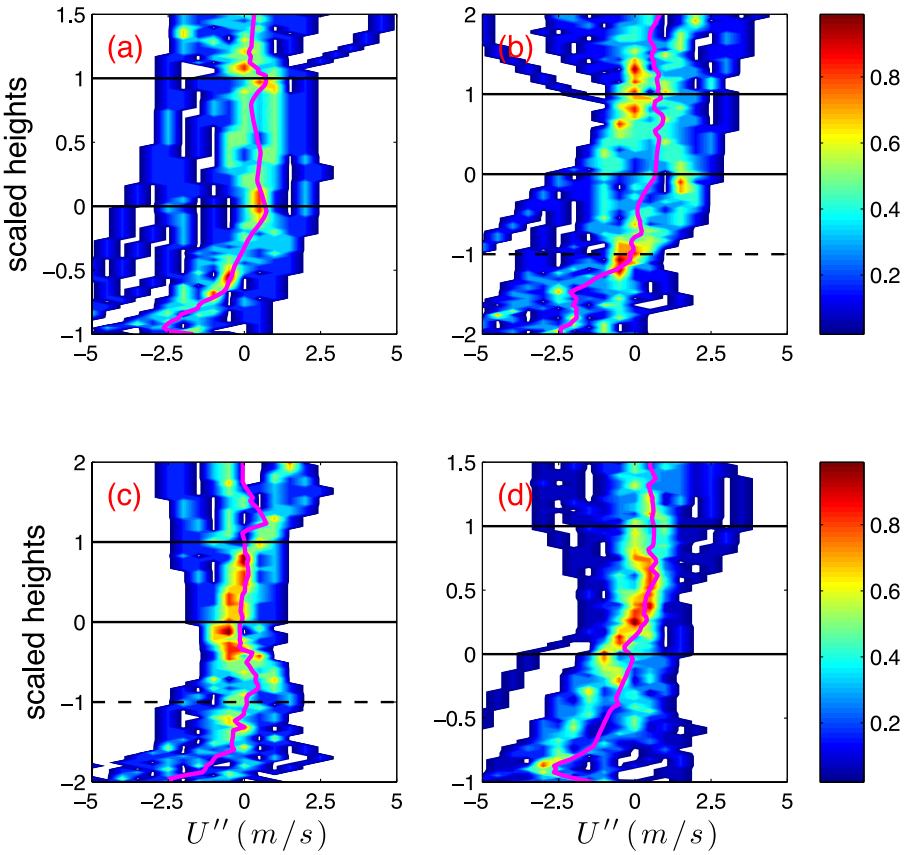

Fig. 20. Same as Fig. 16, but for radiosonde scaled wind speed [m s^{-1}]. See Sect. 3.5 for details on the scaling method.

ACPD
14, 3815–3874, 2014